



This discussion paper is/has been under review for the journal Geoscientific Model Development (GMD). Please refer to the corresponding final paper in GMD if available.

Using the UM dynamical cores to reproduce idealised 3-D flows

N. J. Mayne¹, I. Baraffe¹, D. M. Acreman¹, C. Smith², N. Wood², D. Skålid Amundsen¹, J. Thuburn³, and D. R. Jackson²

¹Physics and Astronomy, University of Exeter, Exeter, EX4 4QL, UK

²Met Office, Exeter, EX1 3PB, UK

³Mathematics, University of Exeter, Exeter, EX4 4QL, UK

Received: 21 June 2013 – Accepted: 1 July 2013 – Published: 12 July 2013

Correspondence to: N. J. Mayne (nathan@astro.ex.ac.uk)

Published by Copernicus Publications on behalf of the European Geosciences Union.

GMDD

6, 3681–3741, 2013

Dynamical cores

N. J. Mayne et al.

Title Page

Abstract

Introduction

Conclusions

References

Tables

Figures



Back

Close

Full Screen / Esc

Printer-friendly Version

Interactive Discussion



Abstract

We demonstrate that both the current (New Dynamics), and next generation (ENDGame) dynamical cores of the UK Met Office global circulation model, the UM, reproduce consistently, the long-term, large-scale flows found in several published idealised tests. The cases presented are the Held–Suarez test, a simplified model of Earth (including a stratosphere), and a model of a hypothetical Tidally Locked Earth (TLE). Furthermore, we show that using simplifications to the dynamical equations, which are expected to be justified for the physical domains and flow regimes we have studied, and which are supported by the ENDGame dynamical core, also produces matching long-term, large-scale flows. Finally, we present evidence for differences in the detail of the planetary (meridional) flows and circulations resulting from improvements in the ENDGame formulation over New Dynamics. Specifically, we find greater symmetry in the meridional circulations of the Tidally Locked Earth test case using the ENDGame formulation, which is a better match to our physical expectations of the flow for such a slowly rotating Earth-like system.

1 Introduction

Global circulation models (GCMs) are used for both numerical weather and climate prediction. The accuracy of predictions made by GCMs of the Earth system are constantly being improved, driven by the requirement to understand our changing climate, improve severe weather warnings for the public, and inform weather sensitive businesses and industries.

The UK Met Office Unified Model (UM) incorporates both weather and climate modeling capabilities in the same code platform. The quality of weather predictions is constantly checked against millions of observations during forecast verification. For climate models pre-industrial control runs are performed and the model is verified against historical observations. The quality of the model is therefore judged on its ability to both

GMDD

6, 3681–3741, 2013

Dynamical cores

N. J. Mayne et al.

Title Page

Abstract

Introduction

Conclusions

References

Tables

Figures



Back

Close

Full Screen / Esc

Printer-friendly Version

Interactive Discussion



produce a good forecast (weather), and to match Earth's recent climate history (climate). Improvements which make the underlying model components more representative of the natural system do not always satisfy both these requirements due to, for instance, compensatory errors.

5 The requirement for accurate climate predictions is becoming increasingly important for Earth as our climate is changing. Additionally, GCMs are also now used for climate modeling of systems other than Earth's future climate. For these cases there is no data assimilation and few independent validating observations. For studies of Earth's palaeoclimate, observational constraints become more uncertain with increasing temporal distance from the present (see for example Lenton et al., 2008). GCMs have also been used to model the climates of other Solar-system planets (see for example models of Jupiter, Saturn, Mars and Venus: Yamazaki et al., 2004; Müller-Wodarg et al., 2006; Hollingsworth and Kahre, 2010; Lebonnois et al., 2011, respectively) where observations exist but are often much harder to interpret and dramatically less numerous than for our own planet. Finally, in the most extreme case, recent detections and observations of exoplanets, or planets outside our own Solar-system, have prompted many groups to begin exploring the possible climate regimes of very distant worlds with GCMs originally designed for the study of Earth's climate (see for example Cho et al., 2008; Showman et al., 2009; Zalucha, 2012). Accordingly, for such cases the primary means of assessing model quality is via a focus on the nature and statistics of the longer term simulated model flow (see Sect. 2 in Held, 2005).

15 This combination of the increasing importance of long term predictions for our own climate, and the extension into new modeling regimes, means that simple testing of climate modeling applications of GCMs is becoming increasingly important. In these cases the exact predictions at a given time are not the best analysis of the quality of the model (unlike weather prediction). The more important aspect of climate models is whether they self-consistently capture the dominant aspects of a climate system under varying conditions, approaching those of the target system (or planetary atmosphere to be studied). Held (2005) has already explained the increasing need for a hierarchy of

Title Page

Abstract

Introduction

Conclusions

References

Tables

Figures



Back

Close

Full Screen / Esc

Printer-friendly Version

Interactive Discussion



Dynamical cores

N. J. Mayne et al.

Title Page

Abstract

Introduction

Conclusions

References

Tables

Figures



Back

Close

Full Screen / Esc

Printer-friendly Version

Interactive Discussion



tests performed on components, or modules, of GCMs as the complexity of models we can feasibly run increases with increasing computing power. This hierarchy includes analytical tests, such as normal mode analysis and the reproduction of analytic flows, as well as more prescriptive tests targeting specific atmospheric phenomena, and extends to statistical analysis of model differences for detailed climate models. Bridging these regimes are tests such as the Held–Suarez test (Held and Suarez, 1994), which is a simplified and idealised experiment isolating the dynamical core (the section which models the evolution of the resolved dynamical flow) of a GCM. This test, and others like it, allow the exploration of model differences or similarities, whilst exploring realistic three dimensional flows run over long periods of elapsed model time. They incorporate a set of simple parameterisations allowing comparison free of the details of, for instance, complicated radiative transfer or boundary layer codes. Such tests increase our confidence in the predictions of GCMs, which is paramount if they are to be used to explore systems where observational constraints are sparse. Furthermore, using idealised tests one can begin to alter aspects of the model to approach the regime we are ultimately interested in. Idealised tests such as the Held–Suarez test are complementary, but not a replacement for, more prescriptive and simplified tests such as the reproduction of analytical flows. Several tests have already been successfully performed using the UM. Most recently, Wood et al. (2013) performed a subset of tests detailed in the Dynamical Core Model Intercomparison Project (DCMIP, see <http://earthsystemcog.org/projects/dcmip-2012/>) and the deep-atmosphere baroclinic instability test of Ullrich et al. (2013). However, these tests evaluate the modeling of specific atmospheric responses, such as gravity waves induced by orography, whereas tests such as Held and Suarez (1994) evaluate the modeled state of the entire atmosphere over long integration times.

We have recently begun a project to model a subset of the most observationally constrained exoplanets using the UM. The subset is termed hot Jupiters as it consists of gas giant planets (of order the mass of Jupiter) which orbit close to their parent star (closer than Mercury is to our Sun). Torques from tidal forces between the star and

Dynamical cores

N. J. Mayne et al.

Title Page

Abstract

Introduction

Conclusions

References

Tables

Figures



Back

Close

Full Screen / Esc

Printer-friendly Version

Interactive Discussion



planet force the planet orbit and rotation into a synchronous state i.e. one year equals one day. This results in a permanent “day” and “night” side (for a review see Baraffe et al., 2010). Their relative brightness and proximity to their host star make observations of some aspects of their atmospheres possible. Most existing GCMs applied to hot Jupiters have used simplified equations of motion (for example Showman et al., 2009; Heng et al., 2011b, use the primitive equations invoking the “shallow-atmosphere” approximation, as well as assuming vertical hydrostatic equilibrium). However, it is probable that several important aspects of these systems, for instance the day–night side heat redistribution and the radius of the hot Jupiter itself (Baraffe et al., 2010; Showman and Guillot, 2002) depend on the detailed dynamics of the atmosphere over many pressure scale-heights. Consequently “shallow”, hydrostatic models may be too simplified to correctly interpret the observations of hot Jupiter atmospheres. Existing work has also already shown the adverse effects of adopting the “traditional” approximation, a component of the “shallow-atmosphere” approximation, and therefore used in the primitive equations, for hot Jupiters (Cho and Polichtchouk, 2011).

The Met Office UM solves the deep, non-hydrostatic equations of motion for the rotating atmosphere, and as part of its continuing development the UM is currently transitioning to a new dynamical core, from New Dynamics (ND, Davies et al., 2005) to ENDGame (Wood et al., 2013). The ENDGame dynamical core provides several improvements on the ND core. For our purposes the most important of these improvements are: better handling of flow across the poles of the latitude-longitude coordinate system; an iterated semi-implicit scheme, providing reduced temporal truncation error; better scaling on multiple processor computer architecture; and an overall improvement of model stability and robustness (Wood et al., 2013). Additionally, the code now includes a set of “switchable” physical assumptions (for instance it can run both with and without the “shallow-atmosphere” approximation, as defined by White et al., 2005, and explained in Table 1). Additionally, a novel mass conserving transport scheme has been developed (SLICE), although for our purposes a standard semi-Lagrangian scheme is used and mass is conserved via a correction factor.

[Title Page](#)[Abstract](#)[Introduction](#)[Conclusions](#)[References](#)[Tables](#)[Figures](#)[Back](#)[Close](#)[Full Screen / Esc](#)[Printer-friendly Version](#)[Interactive Discussion](#)

The ability of the UM to solve the non-hydrostatic deep-atmosphere equations means it is uniquely suited to the study of hot Jupiters. Additionally, the capability of the ENDGame dynamical core to incorporate different simplifications to the dynamics, provides an exceptional tool with which to explore hot Jupiter systems, and determine the importance of the approximations made by previous works modeling such atmospheres. The governing equations of the UM are those best suited (of available GCMs) to modeling hot Jupiters. However, the flow regimes expected in hot Jupiter atmospheres are particularly under constrained, and very different from Earth. Furthermore, the ENDGame dynamical core is not yet operational. Therefore, given the exotic nature of the flow and the use of a developmental code, we require extensive testing. Detailed analytical analysis of the equation set used for the ND and ENDGame dynamical cores has been performed and published (see for example Thuburn et al., 2002a,b), alongside prescriptive tests of atmospheric phenomena (Wood et al., 2013). However, little published testing exists in the regime of idealised three-dimensional flows integrated over long periods, as described previously and in Held and Suarez (1994) and Held (2005). Moreover, existing testing has not been performed on flow regimes with aspects in common with hot Jupiters.

Therefore, we have performed a suite of test-cases using both the ND and ENDGame dynamical cores of the UM ranging from an Earth-type system to a full hot Jupiter system. In this work we present the results for the Earth-type tests namely, the Held–Suarez test (Held and Suarez, 1994), the Earth-like model of Menou and Rauscher (2009) and the Tidally Locked Earth of Merlis and Schneider (2010). These tests progress an Earth-like system, from a simple model, essentially driven by an equator-to-pole temperature difference, to the inclusion of a stratosphere and culminate with the modeling of a longitudinal temperature contrast, which is expected for hot Jupiters. Further development and alterations to the code are required for the modeling of hot Jupiter atmospheres and, therefore, these results will be presented in a subsequent publication.

[Title Page](#)[Abstract](#)[Introduction](#)[Conclusions](#)[References](#)[Tables](#)[Figures](#)[Back](#)[Close](#)[Full Screen / Esc](#)[Printer-friendly Version](#)[Interactive Discussion](#)

The rest of this paper is structured as follows. Section 2 details the key formulations within the ND and ENDGame cores. Then in Sect. 3 we present the results of the test cases and compare the results across the dynamical cores (ND to ENDGame) and after adoption of the various simplifications to the dynamical equations supported by the ENDGame formulation. We also compare with results from literature using independent GCMs. Finally, in Sect. 4 we discuss our results and conclude that the dynamical cores of the UM are both self-consistent and consistent with literature results obtained using other GCMs. As expected invoking the “shallow-atmosphere” approximation does not significantly alter the results for the flow regimes in our Earth-like cases. We find, however, that the detailed meridional flow for the Tidally Locked Earth test case, i.e. over the pole, is different in the ENDGame and ND, which is almost certainly caused by differences in the polar filtering and discretisation, where meridional heat transport is found to be more symmetric (about the equator) for the ENDGame models.

2 Details of dynamical cores

The dynamical cores of the UM, both the ND and ENDGame versions are based on the Non-Hydrostatic Deep formulation (NHD) as described in Staniforth and Wood (2003, 2008), White et al. (2005), Wood et al. (2013). The cores both use a latitude–longitude grid with a terrain following height-based vertical coordinate¹. The cores also have the same underlying horizontal (i.e. an Arakawa-C grid, Arakawa and Lamb, 1977), and vertical (Charney–Phillips grid, Charney and Phillips, 1953) grid structure, and both are semi-implicit and semi-Lagrangian.

2.1 Improvements from ND to ENDGame

Although the equation set and grid staggering are the same in ENDGame and ND, the development of the ENDGame dynamical core includes a large number of changes.

¹Although for this work we include no orography.

In this paper we focus only on the details pertinent to running a set of temperature forced models using the dynamical core. The main changes from ND to ENDGame, with respect to this aim, are explained in this section (a more detailed description of the ENDGame core can be found in Wood et al., 2013).

5 2.1.1 Changes to the formulation

The ND dynamical core has been used operationally for several years and results of simulations run using this core have been presented and discussed in the literature (for example see Walters et al., 2011). The full equation set solved is the NHD incorporating three momentum equations for the zonal, meridional and vertical winds, u , v and w , the continuity and thermodynamic equation, and (in the absence of heating) the equation-of-state. These are:

$$\begin{aligned}
 F^u &= \frac{Du}{Dt} - \frac{uv \tan \phi}{r} + \frac{uw}{r} - 2\Omega v \sin \phi + 2\Omega w \cos \phi + \frac{C_p \theta}{r \cos \phi} \frac{\partial \Pi}{\partial \lambda}, \\
 F^v &= \frac{Dv}{Dt} + \frac{u^2 \tan \phi}{r} + \frac{vw}{r} + 2\Omega u \sin \phi + \frac{C_p \theta}{r} \frac{\partial \Pi}{\partial \phi}, \\
 \delta F^w &= \delta \frac{Dw}{Dt} - \frac{u^2 + v^2}{r} - 2\Omega u \cos \phi + g(r) + C_p \theta \frac{\partial \Pi}{\partial r}, \\
 0 &= \frac{D\rho}{Dt} + \rho \left[\frac{1}{r \cos \phi} \frac{\partial u}{\partial \lambda} + \frac{1}{r \cos \phi} \frac{\partial (v \cos \phi)}{\partial \phi} + \frac{1}{r^2} \frac{\partial (r^2 w)}{\partial r} \right], \\
 \frac{D\theta}{Dt} &= 0, \\
 \Pi^{\frac{1-\kappa}{\kappa}} &= R\rho\theta,
 \end{aligned} \tag{1}$$

where, λ , ϕ , r and t are the longitude, latitude (measured from equator to pole), radial distance from the centre of the planet and time, respectively. Ω , $g(r)$, R , C_p and κ are the rotation rate, gravitational acceleration, gas constant, the heat capacity at constant



pressure, and the ratio R/C_p , respectively. $F^{u,v,w}$ represent sink or source terms for the momenta and δ is a “switch” ($\delta = 0$ or 1) to enable a quasi-hydrostatic equation set (not studied here, see Wood et al., 2013, for explanation). ρ , θ and Π are the density, potential temperature and Exner function (or Exner pressure). θ is given by,

$$\theta = T \left(\frac{\rho_0}{\rho} \right)^{R/C_p}, \quad (2)$$

where T is temperature, ρ is pressure and ρ_0 is the reference pressure, conventionally chosen to be 10^5 Pa, and Π by,

$$\Pi = \left(\frac{\rho}{\rho_0} \right)^{R/C_p} = \frac{T}{\theta}. \quad (3)$$

Finally, the material derivative ($\frac{D}{Dt}$) is given by,

$$\frac{D}{Dt} \equiv \frac{\partial}{\partial t} + \frac{u}{r \cos \phi} \frac{\partial}{\partial \lambda} + \frac{v}{r} \frac{\partial}{\partial \phi} + w \frac{\partial}{\partial r}. \quad (4)$$

Despite solving a set of dynamical equations close to the fully-compressible Euler equations (transformed to a rotating reference frame), i.e. involving very few approximations, some simplifications still remain including:

- Spherical Geopotential (spherical symmetry): $\Phi(\lambda, \phi, r) = \Phi(r)$, where Φ is the geopotential (i.e. the gravitational potential plus the centrifugal contribution). Here the geopotential is constant at a given height (i.e. the latitude and, much smaller, longitude dependencies are dropped, the effect of this assumption is small for the Earth, for a full discussion on geopotentials see White et al., 2008).
- Constant *apparent* Gravity: $g(r) = g_{\text{surf}}$, where g_{surf} is the gravitational constant at the Earth’s surface and is adopted throughout the atmosphere (and ocean). As

Title Page	
Abstract	Introduction
Conclusions	References
Tables	Figures
◀	▶
◀	▶
Back	Close
Full Screen / Esc	
Printer-friendly Version	
Interactive Discussion	



this value is that measured on the Earth's surface (at the equator) the magnitude of the centrifugal component is incorporated. This neglects the contribution of the atmosphere itself to the gravitational potential (self-gravity).

In the ENDGame dynamical core the geopotentials are still approximated as spheres but *the acceleration due to gravity may vary with height*. It is unclear what effect either of these assumptions has on the reliability of weather or climate predictions. White et al. (2005) classify four consistent (i.e. conservative of energy, axial angular momentum and vorticity) equations sets for global atmosphere models. Each equation set involves a different combination of approximations, as detailed in White et al. (2005). Table 1 summarises the main approximations, their effect on the equations of motion and their validity.

If one approximates the atmosphere as a “shallow-fluid” then in order to retain a consistent equation set one must also adopt the “traditional” approximation (White et al., 2005). White et al. (2005), therefore, define the “shallow-atmosphere” approximation as the combination of the “shallow-fluid” and traditional’ approximations (the “traditional” approximation is not invoked based on physical arguments and in fact may be invalid for planetary scale flows, see discussion in White and Bromley, 1995), and also include the assumption of constant gravity, a nomenclature we adopt (see Table 1). This results in a consistent equation set termed the non-hydrostatic shallow-atmosphere equations (NHS). Although the ND dynamical core is based on the NHD equations the constant gravity approximation is still made, essentially meaning the core is based on a pseudo-NHD system. When moving to a shallow, NHS type system the omission of gravity variation is not as immediately inconsistent as adopting a “shallow-fluid” without the “traditional” approximation. White and Wood (2012) explain, in the NHS framework, approximating geopotentials to be spherical leads to a spurious divergence of this potential (which should be zero), which is increased if gravity is allowed to vary with height. A more detailed comparison of the NHS and NHD atmosphere equations and their conservative properties can be found in Staniforth and Wood (2003); White et al. (2005).

Title Page

Abstract

Introduction

Conclusions

References

Tables

Figures



Back

Close

Full Screen / Esc

Printer-friendly Version

Interactive Discussion



[Title Page](#)[Abstract](#)[Introduction](#)[Conclusions](#)[References](#)[Tables](#)[Figures](#)[Back](#)[Close](#)[Full Screen / Esc](#)[Printer-friendly Version](#)[Interactive Discussion](#)

One unique and scientifically useful capability of the ENDGame core is the ability to “switch” the underlying equation set solved, without changing the numerical scheme. ENDGame is capable of solving, within the same numerical framework, either the NHS or NHD equations and further invoking constant or varying gravity (with height). Almost all of the GCMs applied to the study of exoplanets have solved the Hydrostatic Primitive Equations (HPEs White et al., 2005), involving the assumption of vertical hydrostatic equilibrium and a “shallow-atmosphere”. For the test cases studied in this work the assumptions listed in Table 1 are generally valid, or at least have a small effect on the results. When modeling hot Jupiters however, one might expect such approximations to break down, for example, the ratio of the modeled atmospheric extent to planetary radius is much larger (i.e. aspect ratio in this work $\sim 10^{-3}$, but for hot Jupiters ~ 0.1). Therefore, the ability of ENDGame to relax or invoke the canonically made approximations, and thereby cleanly test their impact, will prove vital.

2.2 Changes to the numerical scheme

The ND and ENDGame dynamical cores are both semi-implicit and based on a Crank-Nicolson scheme, where the temporal weighting between the i -th and the $i + 1$ -th state is set by the coefficient α . This leads to a non-linear set of equations which must be solved. The key change to the numerical scheme from ND to ENDGame has been the method of overcoming the non-linearity of the problem, for each atmospheric timestep (or the temporal discretisation used). A nested iteration structure is now used. The *outer* iteration performs the semi-Lagrangian advection (including calculation of the departure points), and values of the pressure increments, from the *inner* iteration are back substituted to obtain updated values for each prognostic variable. The *inner* iteration solves the Helmholtz problem to obtain the pressure increments and the Coriolis and nonlinear terms are updated. There has also been a change in the spatial discretisation such that the meridional velocity is defined at the pole, but no other variable is stored at this location, thereby avoiding the need to solve for pressure at the poles of the latitude-longitude grid (Wood et al., 2013). Thuburn and Staniforth (2004) show that

mass, angular momentum and energy are much more readily conserved with a grid staggered such that v and not u is held at the pole. Additionally, the changes to the spatial and temporal discretisation have led to greater stability at the pole, and have removed the need, in most cases, for polar filters. For cases where v becomes significant (as demonstrated in Sect. 3.5) a “sponge layer” (Klemp and Dudhia, 2008; Melvin et al., 2010) has been implemented which allows damping of vertical velocity (usually from gravity or acoustic waves), which can be used as part of the upper boundary condition and extend down to the surface at each pole.

3 Test cases

As part of our project to model exoplanets we have installed the externally released UM VN7.9, using the ND dynamical core and VN8.2, adapted to use the developmental ENDGame dynamical core. We have, in order to check the veracity of our version of the code and test regimes approaching our target systems of hot Jupiters, then run each version through a set of test cases. These test cases isolate the dynamical core and solve for the atmosphere only, in the absence of orography. The test cases presented in this work are the original (simple) Held–Suarez test (HS, Held and Suarez, 1994), a simple Earth-Like model including a stratosphere (EL, Menou and Rauscher, 2009) and a hypothetical Tidally Locked Earth, allowing the opportunity to explore the model performance with a longitudinal temperature contrast (TLE, Merlis and Schneider, 2010; Heng et al., 2011b).

For these tests radiative transfer is parameterised using simple temperature forcing to a prescribed temperature profile. “Newtonian cooling” is prescribed as

$$Q_{\text{Newton}} = \frac{T_{\text{eq}} - T}{\tau_{\text{rad}}}, \quad (5)$$

where, T_{eq} is the prescribed equilibrium temperature profile, T the current temperature and τ_{rad} the characteristic radiative or relaxation timescale. τ_{rad} (and therefore Q_{Newton})

Title Page

Abstract

Introduction

Conclusions

References

Tables

Figures



Back

Close

Full Screen / Esc

Printer-friendly Version

Interactive Discussion



can be set as constant or as a function of pressure or height. Practically, each timestep the temperature² is then shifted (as a “slow” physics process) towards the equilibrium temperature using,

$$T^{i+1} = T^i - \frac{\Delta t}{\tau_{\text{rad}}}(T^i - T_{\text{eq}}), \quad (6)$$

5 where superscript indicates the timestep, and Δt is the length of the timestep (see Table 3). Boundary layer friction is also represented using a simple “Rayleigh friction” scheme, where the horizontal winds are damped close to the surface (again as a “slow” physics process),

$$u^{i+1} = u^i - \frac{\Delta t}{\tau_{\text{fric}}}u^i, \quad (7)$$

10 (and similarly for v) where τ_{fric} is the characteristic friction timescale. Therefore, each test case prescribes three “profiles”: an equilibrium temperature, relaxation or radiative timescale and horizontal frictional timescale profile.

Finally, each model has also been run including a very simple dry static adjustment of θ to remove any convective instability. As the condition for convective instability is $\frac{d\theta}{dz} < 0$, each column is examined for negative vertical potential temperature gradients after each timestep. If a column is found to be convectively unstable $\theta(z)$ is re-arranged, i.e. the temperature in the column is just rearranged to ensure stability³.

3.1 Models run

20 We have run each test case using ND and ENDGame. We have also run each test case using ENDGame but varying the set of simplifications or assumptions to the dynamical

²The code actually uses potential temperature as a prognostic, thermodynamic variable, but the process is equivalent as it is performed at fixed Π .

³The effect of including a convective adjustment scheme has been explored for several Earth-like test cases by Heng et al. (2011a).

Title Page

Abstract

Introduction

Conclusions

References

Tables

Figures

◀

▶

◀

▶

Back

Close

Full Screen / Esc

Printer-friendly Version

Interactive Discussion



equations. Table 2 shows the names we use to refer to different model setups, the dynamical core used, the underlying equation set and the associated approximations (the approximations are as discussed in Sect. 2.1.1 and presented in Table 1).

The model EG_{gc} setup was chosen explicitly to match the ND equations, and thereby allow us to potentially isolate differences in solution caused by changes in the numerical scheme between the dynamical cores. These runs are compared and discussed for each test case in turn, alongside comparison to the original test, in this section. These practical tests complement the analysis of normal modes in Thuburn et al. (2002a,b), and standardised flow tests (e.g. Ullrich et al., 2013; Wood et al., 2013). The general parameters for the model runs are listed in Table 3.

3.2 Vertical coordinate & methods of model comparison

The literature sources, presenting the test cases we study in this work, all used GCMs which adopt pressure or σ as their vertical coordinate ($\sigma = \frac{p}{p_{\text{surf}}}$, where p_{surf} is the surface pressure), whereas the UM is height-based. This creates some barriers to a clean comparison between our models and the literature examples. Firstly, the boundary conditions (and therefore model domain) can only be approximately matched. Secondly, our vertical resolutions, and more specifically, level placements will be different. Finally, to explicitly compare the results we must transform our results to σ space.

Our upper boundary, being constant in height, will experience fluctuations in pressure⁴. Practically, the initial pressure of the inner boundary (or surface) is set and a domain large enough so as to reach the lowest required pressure is selected. Therefore, if the horizontal or temporal pressure gradients are significant our model domain will not match that of a pressure based model, where the upper boundary is a constant pressure surface. While this is not the case for the tests in this work, for our work on hot Jupiters changes in the pressure on the top boundary can lead to a significant change in the physical size of the domain (Mayne et al., 2013). The distribution of levels within

⁴In most pressure-based models the inner boundary is still a constant height surface.

Title Page

Abstract

Introduction

Conclusions

References

Tables

Figures



Back

Close

Full Screen / Esc

Printer-friendly Version

Interactive Discussion



[Title Page](#)[Abstract](#)[Introduction](#)[Conclusions](#)[References](#)[Tables](#)[Figures](#)[Back](#)[Close](#)[Full Screen / Esc](#)[Printer-friendly Version](#)[Interactive Discussion](#)

our domain can then be selected to sample the associated σ space evenly to match the literature models. Practically, for each test case we run a model with a (moderate resolution) uniform grid over a domain extending to pressures lower than sampled in the original, literature, σ model. Zonal and temporal averages are then used to create a set of level heights (and an upper boundary position) to emulate even σ sampling. We have also, when compared to the literature models we examine, increased our number of vertical levels to ensure sufficient resolution. The resulting level heights for each test case are presented in Table A1 in dimensionless height coordinates, alongside the approximate σ value of each level.

Comparison of our models with literature results then requires additional conversion. Although our level and boundary placements have been selected to better sample the required σ space we still use geometric height as our vertical coordinate. Therefore, for each completed test case, the pressure (and therefore σ) values are found and the prognostic variable is interpolated (at every output timestep) into σ space.

To determine a satisfactory match of the mean, large-scale, long term structure of our modeled atmospheres with literature results, we compare the prognostic fields of velocity and temperature. These fields are averaged (using a mean) in the diagnostic plots of the original publications in both time and space. Additional care must be taken when performing spatial averaging and comparing models across different vertical coordinates (as discussed in the Appendix of Hardiman et al., 2010). Where we are comparing directly to a literature figure or result we perform the spatial averaging in σ space. The required prognostic field is (as discussed above) interpolated from the height grid onto a σ grid, and then the average performed along constant σ surfaces, to allow the most consistent comparison with literature, σ -based models. To further enhance the comparison of our results with those in the literature, where possible the line contours (solid lines for positive values and dotted lines for negative) presented in the plots of our model results have been chosen to match the original publications. We have then, to aid a qualitative interpretation of our models, complemented the line contours with additional (more numerous) colour contours. For plots showing wind or

[Title Page](#)[Abstract](#)[Introduction](#)[Conclusions](#)[References](#)[Tables](#)[Figures](#)[Back](#)[Close](#)[Full Screen / Esc](#)[Printer-friendly Version](#)[Interactive Discussion](#)

circulation patterns the coloured contours are separated at zero (where blue represents negative flow, and red positive⁵), again to aid visual presentation of the flow. Each of the original publications introducing the tests we have performed include the comparison of additional quantities (for example the eddy temperature and wind variance in Held and Suarez, 1994). In this work, however, for brevity (as we are performing several tests) we compare only the prognostic variable fields, i.e. wind and temperature, complemented by comparison of the Eddy Kinetic Energy (EKE) defined as

$$\text{EKE} = \frac{(u'^2 + v'^2)}{2}, \quad (8)$$

where the prime denotes a perturbation such that $u' = u - \overline{u}^{\lambda_z, t}$, where $\overline{u}^{\lambda_z, t}$ is the variable averaged (mean) in longitude (λ) and time (t). One critical difference with this quantity (compared to the others we plot) however, is that the spatial (zonal) average is performed in height coordinates (hence the subscript z). Therefore, plots of EKE will be presented in height not σ space. This is done as we compare the zonal and temporal mean of the EKE, i.e. $\overline{\text{EKE}}^{\lambda_z, t}$. Given that the perturbation itself is constructed from a spatial and temporal mean, we are performing several averaging processes and it is simpler and more intuitive to keep the variable in the natural coordinate system of the model. Moreover, in the case of EKE, we are actually comparing only our own models with each other, not with a literature σ -based model. The EKE then allows us to explore differences in the eddy structures of the models, complementary to the plots depicting the relatively insensitive means of the wind and temperature fields. Additional details regarding the comparison between our work and that of Heng et al. (2011b) can be found in Appendix A1.

⁵The splitting means that the red and blue colour scales need not be symmetric about zero.

3.2.1 Initial conditions

As stated in Held and Suarez (1994), for their HS test an initial spin-up time of 200 days is used to effectively allow the system to reach a statistically steady-state and erase the initial conditions. This is why *temporal average* (whenever it is stated as being performed) means the average of the field from 200 to 1200 days. Our adopted initial conditions were a simple, hydrostatically balanced, isothermal atmosphere (temperature presented in Table 3) with zero u, v and w velocities.

3.3 Held–Suarez

The HS test prescribes an equilibrium temperature profile of

$$T_{\text{eq}} = \max\{T_{\text{stra}}, T_{\text{HS}}\}, \quad (9)$$

where,

$$T_{\text{HS}} = \left[T_{\text{surf}} - \Delta T_{\text{EP}} \sin^2 \phi - \Delta T_z \ln \left(\frac{\rho}{\rho_0} \right) \cos^2 \phi \right] \left(\frac{\rho}{\rho_0} \right)^{\kappa}, \quad (10)$$

and, $T_{\text{stra}} = 200 \text{ K}$, $T_{\text{surf}} = 315 \text{ K}$, $\Delta T_{\text{EP}} = 60 \text{ K}$, $\Delta T_z = 10 \text{ K}$ and $\rho_0 = 1 \times 10^5 \text{ Pa}^6$. The radiative timescale is modeled as,

$$\frac{1}{\tau_{\text{rad}}} = \frac{1}{\tau_{\text{rad, d}}} + \begin{cases} 0, & \sigma \leq \sigma_b, \\ \left(\frac{1}{\tau_{\text{rad, u}}} - \frac{1}{\tau_{\text{rad, d}}} \right) \left(\frac{\sigma - \sigma_b}{1 - \sigma_b} \right) \cos^4 \phi, & \sigma > \sigma_b, \end{cases} \quad (11)$$

where, $\tau_{\text{rad, d}} = 40$ days, $\tau_{\text{rad, u}} = 4$ days and $\sigma_b = 0.7$ (the top of the surface friction boundary layer).

⁶All units used are SI units.

The boundary layer horizontal wind damping enforces a damping on a timescale, τ_{fric} given by:

$$\frac{1}{\tau_{\text{fric}}} = \begin{cases} 0, & \sigma \leq \sigma_b, \\ \left(\frac{1}{\tau_{\text{fric},f}}\right) \left(\frac{\sigma - \sigma_b}{1 - \sigma_b}\right), & \sigma > \sigma_b, \end{cases} \quad (12)$$

where, $\tau_{\text{fric},f} = 1$ day.

Figures 1 and 2 show the zonally (along constant σ surfaces) and temporally averaged zonal wind and temperature ($\bar{u}^{\lambda\sigma,t}$ and $\bar{T}^{\lambda\sigma,t}$), respectively, from the original (Held and Suarez, 1994) publication, and from our ND and ENDGame setups.

Qualitatively, both the ND (middle panel) and the EG (bottom panel) temperature and zonal wind fields (when averaged zonally and temporally) match the original Held and Suarez (1994) (top panel) results of the finite difference model. However, the 210 K contour (Fig. 1), and the wind contours extending over the poles, and over the equator (Fig. 2) show a slightly better match with Held and Suarez (1994) when moving from the ND to the ENDGame models (however these flows represent very small velocities $\lesssim 1 \text{ ms}^{-1}$). The ND model shows a slightly different vertical temperature profile for the lowest levels, when compared to the EG model. This is caused by differences in the temperature modeled in the lowest grid cell. The ENDGame model records the temperature, in the atmosphere array, down to the surface, whereas ND does not. Therefore, for display purposes the potential temperature across the bottom cell has been estimated to be constant in the ND model, resulting in a slight increase of temperature (as $T = \Pi\theta$ and the lowest $\sigma \sim 0.97$, and by definition $\sigma_{\text{surf}} \equiv 1$, see Table A1).

Figure 3 shows zonally and temporally averaged zonal wind plots for all of the ENDGame models (namely, EG, EG_{gc} and EG_{sh}, where EG has been presented already in Fig. 2 but is reproduced in Fig. 3 to aid visual comparison). The similarity of the panels of Fig. 3 shows that, as expected for such a domain and flow regime (i.e. the lack of large, in vertical extent, circulation cells), making the “shallow-atmosphere” approximation (or approximating gravity as a constant only) does not significantly affect

Title Page

Abstract

Introduction

Conclusions

References

Tables

Figures



Back

Close

Full Screen / Esc

Printer-friendly Version

Interactive Discussion



[Title Page](#)[Abstract](#)[Introduction](#)[Conclusions](#)[References](#)[Tables](#)[Figures](#)[◀](#)[▶](#)[◀](#)[▶](#)[Back](#)[Close](#)[Full Screen / Esc](#)[Printer-friendly Version](#)[Interactive Discussion](#)

similar for all models. However, the results of the ND model shows, with respect to the ENDGame plots, an increase in the EKE at $\phi \sim 50^\circ$ towards the upper boundary (i.e. coincident with the peak wind speed of the prograde jets). To illustrate the difference explicitly we show in Fig. 6, as with the temperature and zonal wind fields, the differences of the $\overline{\text{EKE}}^{\lambda_z t}$ for each model. Specifically, Fig. 6 shows difference in $\overline{\text{EKE}}^{\lambda_z t}$ in the sense EG–ND, EG–EG_{gc} and EG–EG_{sh}, as the top, middle and bottom rows respectively. In Fig. 6 the line contours have been chosen to be the same for all panels.

Figure 6 shows, for the EG model compared to ND (top panel), more kinetic energy associated with the eddy component of the flow over the equator, and near the surface at a latitude associated with the peak zonal wind speed ($\phi \sim 50^\circ$). The magnitude of the peak relative differences in $\overline{\text{EKE}}^{\lambda_z t}$ are ~ 1.65 , 0.36 and 0.42 for the differences EG–ND, EG–EG_{gc} and EG–EG_{sh}, respectively. There is a decrease in EKE found in the EG model when compared to the ND model higher in the atmosphere. Comparing EG to EG_{gc} (middle panel) again shows more kinetic energy associated with eddies in the EG model, over the equator, at high altitudes, however, the differences associated with the mid-latitude jets now appear over similar altitudes. Finally, the difference EG–EG_{sh} (bottom panel) shows a similar spatial pattern to EG–EG_{gc} but the signs are reversed. Overall, Fig. 6 shows that detailed, eddy, component of the flow, can be quite different, although not affecting the diagnostic plots (for example Figs. 1 and 2) significantly.

3.4 Earth-like

For the Earth-Like test case of Menou and Rauscher (2009), the temperature profile includes a parameterised stratosphere,

$$T_{\text{eq}} = T_{\text{vert}} + \beta_{\text{trop}} \Delta T_{\text{EP}} \left(\frac{1}{3} - \sin^2 \phi \right) \quad (13)$$

where

$$T_{\text{vert}} = \begin{cases} T_{\text{surf}} - \Gamma_{\text{trop}} \left(z_{\text{stra}} + \frac{z - z_{\text{stra}}}{2} \right) \\ + \left(\left[\frac{\Gamma_{\text{trop}} (z - z_{\text{stra}})}{2} \right]^2 + \Delta T_{\text{strat}}^2 \right)^{\frac{1}{2}}, & z \leq z_{\text{stra}}, \\ T_{\text{surf}} - \Gamma_{\text{trop}} z_{\text{stra}} + \Delta T_{\text{strat}}, & z > z_{\text{stra}}, \end{cases} \quad (14)$$

and $T_{\text{surf}} = 288 \text{ K}$ is the surface temperature, $\Gamma_{\text{trop}} = 6.5 \times 10^{-3} \text{ K m}^{-1}$ is the lapse rate, and $\Delta T_{\text{strat}} = 2 \text{ K}$, an offset to smooth the transition from the troposphere (finite lapse rate) to the isothermal stratosphere. z_{stra} and σ_{stra} are then the locations in height and σ of the tropopause. β_{trop} is defined as

$$\beta_{\text{trop}} = \begin{cases} \sin \frac{\pi(\sigma - \sigma_{\text{stra}})}{2(1 - \sigma_{\text{stra}})}, & z \leq z_{\text{stra}} \quad \text{or} \quad \sigma \geq \sigma_{\text{stra}}, \\ 0, & z > z_{\text{stra}} \quad \text{or} \quad \sigma < \sigma_{\text{stra}}. \end{cases} \quad (15)$$

The remaining parameters match those of HS, except, here the radiative timescale is set as a constant, $\tau_{\text{rad}} = 15 \text{ days}$, but, following Heng et al. (2011b) the same ‘‘Rayleigh friction’’ scheme as for HS is implemented (this differs from the choice of Menou and Rauscher, 2009, where only the bottom level winds are damped which creates a resolution dependent damping profile).

Figure 7 shows the zonally averaged (in σ space) zonal wind and temperature fields for our ND and EG models, and the results from Heng et al. (2011b), both have been temporally averaged (i.e. $\bar{u}^{\lambda, t}$ and $\bar{T}^{\lambda, t}$). Our models are in excellent agreement with the results of Heng et al. (2011b) (although we have slightly stronger high-altitude components of the mid-latitude jets). Our results also match the ‘‘snapshots’’ of the flow field presented in Menou and Rauscher (2009). This agreement again, as found with the HS test, suggests sufficient vertical resolution (15, 20 and 32 vertical levels used in Menou and Rauscher, 2009; Heng et al., 2011b, and this work, respectively).

[Title Page](#)[Abstract](#)[Introduction](#)[Conclusions](#)[References](#)[Tables](#)[Figures](#)[Back](#)[Close](#)[Full Screen / Esc](#)[Printer-friendly Version](#)[Interactive Discussion](#)

Further evidence of the extrapolation of the temperature down to the surface of the ND model, performed as part of the visualisation process, is apparent in the right panels of Fig. 7, in the contours close to the surface. The left panels of Fig. 7 shows a slight improvement in the agreement of the flow structure at high and low latitudes, between the results of Heng et al. (2011b) and our own model when moving from ND to EG. Figure 8 then shows the temporally and zonally averaged zonal wind for the three versions of the ENDGame models. The qualitative agreement between all the panels in Fig. 8 again shows that the assumptions are valid, and that the code is consistently solving for the long-term and large-scale 3-D flow. There are only very slight differences, for example, as we move towards a more simplified model (i.e. downwards in Fig. 8) we generally see the edge of 3.6 ms^{-1} contour moving to higher latitudes, and a slight degradation in the symmetry of the flow. Additionally, all of the ND and ENDGame models show a greater hemispherical symmetry in the wind patterns than the finite difference model presented in Heng et al. (2011b), and, in fact, match the levels of symmetry present in the results of the spectral code of Heng et al. (2011b) (not shown here).

Again, as with the HS test case in Sect. 3.3 the different ENDGame models show negligible differences in the results, so only the difference EG–ND is shown in Fig. 9. The format of Fig. 9 matches that of Fig. 4. Figure 9 shows a similar, yet reduced in magnitude, pattern to that present in Fig. 4, with a warmer upper atmosphere showing enhanced flow, and cooler mid-atmosphere, in the EG model over the ND model.

Again, to explore the eddy component of the flow, Fig. 10 shows the EKE, zonally (along geometric height surfaces) and temporally averaged ($\overline{\text{EKE}}^{\lambda_z t}$), for the ND and all ENDGame models. Figure 10, as in Fig. 5 shows qualitative agreement with the overall pattern of $\overline{\text{EKE}}^{\lambda_z t}$, however in this case the peak value is much larger for the ND model (compared to any ENDGame model). The magnitude of the peak relative differences in $\overline{\text{EKE}}^{\lambda_z t}$ are ~ 2.0 , 0.80 and 0.46 for the differences EG–ND, EG–EG_{gc} and EG–EG_{sh}, respectively, slightly larger than found in the HS case. The ENDGame models also

show more structure along the peak of $\overline{\text{EKE}}^{\lambda_z, t}$ activity and the “lobes” equator ward of the peak.

To emphasise the slight differences in $\overline{\text{EKE}}^{\lambda_z, t}$ apparent in Fig. 10 we present a difference plot, for EG–ND only (as the differences between the ENDGame models are an order of magnitude smaller), in Fig. 11.

There is a significant reduction in variation in the $\overline{\text{EKE}}^{\lambda_z, t}$ across all of the EL models, when compared to the HS test case (see Figs. 5 and 10), as the EL test is a simpler flow regime to capture. The EG–ND of $\overline{\text{EKE}}^{\lambda_z, t}$, in Fig. 11 also shows the peak difference is close to the upper boundary, coincident in latitude, with the peak of the prograde jets.

3.5 Tidally Locked Earth

For the Tidally Locked Earth (TLE) test of Merlis and Schneider (2010) we slow the rotation rate so that a day is now equal to an orbital period (i.e. a year), $\Omega \rightarrow \frac{\Omega}{365}$. This introduces a longitudinal temperature contrast and allows us to test the model behaviour in a familiar system (i.e. Earth) but incorporating aspects found in the hot Jupiter atmospheric regime. We have not included moisture in the calculation and therefore, have essentially, performed the simplified version of the test which is described and performed by Heng et al. (2011b). The equilibrium temperature profile is then a modified version of the HS profile, enforcing a longitudinal temperature contrast and “hot spot” at the subsolar point centred at a longitude of 180° (and latitude of zero). It is given by:

$$T_{\text{eq}} = \max\{T_{\text{stra}}, T_{\text{TLE}}\}, \quad (16)$$

where,

$$T_{\text{TLE}} = \left[T_{\text{surf}} + \Delta T_{\text{EP}} \cos(\lambda - 180^\circ) \cos \phi - \Delta \theta_z \ln \left(\frac{\rho}{\rho_0} \right) \cos^2 \phi \right] \left(\frac{\rho}{\rho_0} \right)^\kappa. \quad (17)$$

The parameters and values in common with the HS model take the same values.

Title Page

Abstract

Introduction

Conclusions

References

Tables

Figures

⏪

⏩

◀

▶

Back

Close

Full Screen / Esc

Printer-friendly Version

Interactive Discussion



However, for this model, where significant flow over the pole exists, we must add a sponge layer into the ENDGame formulation for model stability (ND incorporates a polar filter). This damps vertical motions and is explained in Klemp and Dudhia (2008); Melvin et al. (2010). The damping term R_w (included in the solution for vertical velocity) is,

$$w^{t+\Delta t} = w^t + S_w - R_w \Delta t w^{t+\Delta t}, \quad (18)$$

where w^t and $w^{t+\Delta t}$ are the vertical velocities at the current and next timestep, S_w a source term, and Δt the length of the timestep (as before). The spatial extent and value of the damping coefficient (R_w) is then determined by the equation

$$R_w = \begin{cases} C \left(\sin^2 \left(0.5\pi(\eta - \eta_s) \left(\frac{1.0}{1.0 - \eta_s} \right) \right) + \sin^{40}(\phi) \right), & \eta \geq \eta_s \\ 0, & \eta < \eta_s, \end{cases} \quad (19)$$

where, given the absence of orography, $\eta = \frac{z}{H}$ (i.e. non-dimensional height, where H is the height of the upper boundary), η_s is the start height for the top level damping (set to $\eta_s = 0.75$) and C is a coefficient (set to 0.05).

Figure 12 is a reproduction of the grid-based model results for the TLE test in Heng et al. (2011b). It shows the temperature at the $\sigma = 0.975$ surface at 1200 days (top panel), the temporally averaged zonal wind (\bar{u}^t) at the surfaces $\sigma = 0.225, 0.525$ and 0.975 (in descending panel order)⁷.

Figure 13 shows the same type of plots as Fig. 12, but constructed using the ND (left panels) and EG (right panels) models, where the other ENDGame models are omitted as the results are negligibly different from the EG model.

Figure 14 is a reproduction of the results of the grid-based model for the TLE test case of Heng et al. (2011b), showing the temporally averaged meridional velocity (\bar{v}^t) at $\sigma = 0.225, 0.525$ and 0.975 (from top to bottom panel, respectively).

⁷See discussion in Appendix A1 for explanation of differences in quoted σ levels between our work and that of Heng et al. (2011b).

Title Page

Abstract

Introduction

Conclusions

References

Tables

Figures

◀

▶

◀

▶

Back

Close

Full Screen / Esc

Printer-friendly Version

Interactive Discussion



[Title Page](#)[Abstract](#)[Introduction](#)[Conclusions](#)[References](#)[Tables](#)[Figures](#)[Back](#)[Close](#)[Full Screen / Esc](#)[Printer-friendly Version](#)[Interactive Discussion](#)

The results for our models are shown in Fig. 15 in the same vertical format as Fig. 14. As for Fig. 13 the figures show the ND (left panels) and EG (right panels) models, where (as with Fig. 13) the other ENDGame models are omitted as the results are negligibly different from the EG model.

Comparison of the results of Heng et al. (2011b), Figs. 12 and 14 with our results, Figs. 13 and 15 reveals qualitative agreement. Again, as before our vertical resolution is higher than that of Heng et al. (2011b), 32 as opposed to 20 levels. So the agreement not only shows that the ENDGame dynamical core produces consistent flows both with other GCMs and the ND dynamical core, but also that the change in vertical resolution is unimportant (differences are discussed later in this section). Tentative evidence for a smoother modeling of the meridional flow can also be seen by comparing our results for the v field (Fig. 15) at a σ of 0.225 and 0.525 to that of Heng et al. (2011b) (Fig. 14). Our figures produce flow contours less featured than those of Heng et al. (2011b) (in fact our model matches more closely the spectral model results not reproduced here which we expect to be more accurate for large-scale flows, compared to the finite-difference model). Additionally, as with the previous cases, given the model domain one would expect little difference in results whether the “shallow-atmosphere” approximation is made or not (given the aspect ratio, height over the length scale, $H/L \sim \frac{3.2 \times 10^4}{2.0 \times 10^7} \sim 10^{-3}$, where the length scale is chosen as half the perimeter of the planet due to the presence of hemispherical circulation cells), and gravity does not vary much over the atmosphere ($g_{\text{surf}} \sim 9.8 \text{ ms}^{-1}$ at the surface to $g(r_{\text{top}}) = g_{\text{surf}}(R_p/r_{\text{top}})^2 \sim 9.8 \times \left(\frac{6.4 \times 10^6}{[3.2 \times 10^4 + 6.4 \times 10^6]}\right)^2 \sim 0.990 \times 9.8 \text{ ms}^{-1}$, at the top of the atmosphere ignoring self-gravity and using the inverse square-law).

The level of consistency, of the horizontal flow, across all of the ENDGame models for the resulting TLE flow is excellent. Further evidence for a consistent solution can be found in the similarity of the time averaged vertical velocities over the “hot spot”. These are shown in Fig. 16 for EG_{sh} and EG models.

[Title Page](#)
[Abstract](#)
[Introduction](#)
[Conclusions](#)
[References](#)
[Tables](#)
[Figures](#)

[Back](#)
[Close](#)
[Full Screen / Esc](#)
[Printer-friendly Version](#)
[Interactive Discussion](#)


in the spectral code models of Heng et al. (2011b) (see Figs. 3 and 4 of Heng et al., 2011b), which does not include any polar filtering. The fact that the ENDGame models match the results of the spectral code more closely (than the finite-difference version) is an excellent indication that explicit polar damping scheme used in the ND model is responsible for the change in flow structure at $\sigma = 0.525$.

The structure of the “hot spot” in the top panel of Fig. 13 shows the central contour is more elliptical for all the ENDGame solutions, matching more closely (than the ND models) the shape in Fig. 12. The structure of the “hot spot” also seems “noisier” in the ENDGame models. The noise exhibited in the ENDGame models is indicative of the reduced implicit damping in the numerical scheme. This can be shown by making the ENDGame scheme more implicit, and therefore, dissipative, by adjusting the temporal weighting coefficient, α . Increasing α leads to greater weight being applied to the $i + 1$ state and therefore a more implicit scheme. For our ND model and all ENDGame models the α values are 0.7 and 0.55 respectively (i.e. ENDGame is more explicit, yet is able to run stably with the same length timestep due to the changes outlined in Sect. 2.2 and detailed in Wood et al., 2013). Figure 18 shows the temperature structure shown in Fig. 13 (top panel) for both the EG using the standard $\alpha = 0.55$ (already displayed in Fig. 13, rightmost panel, reproduced to aid comparison) and an EG model where α has been increased to 1.0. The fully implicit model presents a smoother temperature structure.

To attempt to isolate differences caused only by the numerical scheme we compare the nature of the meridional circulation for the TLE models using ND and EG_{gc}, since the ND and EG_{gc} models solve identical equations sets. Figure 19 shows the temporally and meridionally averaged meridional flow for the ND and EG_{gc} models. The average is performed in a point-wise fashion, i.e. $\int v d\phi$ as opposed to $\int \cos\phi v d\phi$, to emphasise differences in flow over the pole caused by the necessity for a polar filter in the ND models. In a non-rotating system, where the Coriolis force is zero, one would expect a symmetric meridional flow, so the latitudinal average should be close to zero. For the TLE case the rotation is slow, with a Rossby number of, $Ro = \frac{U}{L\bar{f}} \sim \frac{30}{4 \times 10^7 \times 2 \times 2 \times 10^{-7}} \sim$

2.0 (where U is the horizontal velocity scale, L the length scale and $f = 2\Omega \sin \phi$; the Coriolis frequency or parameter), indicating negligible effects of rotation.

Figure 19 shows that the meridional average is almost an order of magnitude larger in the ND case, compared with the EG_{gc} model. To further examine the symmetry of meridional circulation cells, we define a stream function (Ψ) as

$$\Psi = -2\pi \cos \phi \int_{R_p}^r r \bar{v}(\phi, \tilde{r}) d\tilde{r}, \quad (20)$$

where \bar{v} denotes the zonally averaged meridional velocity.

Figure 20 shows this diagnostic as a function of latitude and height for the ND and EG_{gc} models. The values assigned to the contours in both panels of Fig. 20 are the same. The results are similar for both models but the circulation cells are somewhat more symmetric (especially closer to the surface) for the EG_{gc} models. The lower (in altitude) circulation cells are *direct* i.e. caused by the heating of the atmosphere, whilst the higher cells are *indirect*. As shown in Heng et al. (2011a) the circulation cells differ on the day and night side. However, here we do not split by hemisphere as we are simply interested in the comparison between models.

Figure 21 shows the EKE, zonally (along geometric height surfaces) and temporally averaged ($\overline{EKE}^{\lambda_z t}$), for the ND and all ENDGame models. Figure 21 shows more distinct differences when comparing ND to any of the ENDGame models, compared to the HS or EL test cases. In the TLE case the kinetic energy associated with the eddies clearly increases when moving from ND to ENDGame. Additionally, the structure of the peak activity region, which extends from mid-latitudes over the poles, is flatter (in altitude) in the ENDGame models. One of the main reasons the total EKE reduces from the ENDGame to the ND model is due to the polar filtering applied in the ND model (and absent from the EG model), as the EKE is generally concentrated over the pole. One can also observe a move to increased hemispherical symmetry when moving from ND through EG_{sh} and EG_{gc} to EG. This shows that ENDGame produces

[Title Page](#)[Abstract](#)[Introduction](#)[Conclusions](#)[References](#)[Tables](#)[Figures](#)[Back](#)[Close](#)[Full Screen / Esc](#)[Printer-friendly Version](#)[Interactive Discussion](#)

found for the results of these three idealised test cases, both between the UM dynamical cores and when compared with literature results. Furthermore, the consistency of the solutions was not changed when invoking the approximations possible in the ENDGame equation set, all of which should be applicable for our test cases, namely, the “shallow-atmosphere” approximation, as a whole, or just the assumption of constant gravity. We also found tentative evidence of differences in the meridional flow between the ENDGame and ND cores caused by the temporal and spatial discretisation and removal of the polar filter (although a sponge layer for the vertical velocity component was used for the ENDGame models).

These results should be viewed as complementary to more analytical testing. For our project, namely adapting the UM with a state-of-the-art dynamical core to exoplanets, this work is a crucial first step in confirming the consistency of the code, both with other GCMs and, under different approximations to the full equations of motion. We have also tested the code in flow regimes with features in common with the subset of exoplanets termed hot Jupiters (which our project aims to characterise), i.e. a hypothetical Tidally Locked Earth. For the flow regimes of hot Jupiters the solutions to the equations of motion are expected to differ under the different approximations featured in this work. Furthermore, these objects are severely observationally under-constrained, so rigorous testing is required. We will present the next step of this project, involving adaptation of the code and simplified giant planet test cases in a future work (Mayne et al., 2013).

Appendix A

A1 A note on comparison with the work of Heng et al. (2011b)

Heng et al. (2011b) perform both finite-difference and spectral models of the test cases using the same GCM (the Princeton Flexible Modeling System, FMS). In this work we concentrate our comparison with the results of the finite-difference versions of the test,

[Title Page](#)[Abstract](#)[Introduction](#)[Conclusions](#)[References](#)[Tables](#)[Figures](#)[Back](#)[Close](#)[Full Screen / Esc](#)[Printer-friendly Version](#)[Interactive Discussion](#)

as the UM also adopts a finite-difference method. Additionally, it is not clear which σ surface Heng et al. (2011b) select when producing plots of the atmosphere as a function of latitude and longitude, in the spectral case. The spectral version of the FMS dynamical core performs vertical finite-differencing using a Simmons-Burridge scheme.

Heng et al. (2011b) state, the prognostic variable output is not exactly at the mid-point of the vertical half-levels, and when presenting results they usually quote the σ of the bottom pair of half-levels. Therefore, some uncertainty exists over which σ surface the resulting plots are produced from. For the finite-difference results Heng et al. (2011b) state that the labeling of the model layers adopts the same system as the spectral version, i.e. each layer is actually labeled with the value of the larger σ half-level. This may result in a slight translation, or vertical shift, when we present plots with σ as the vertical axis. As comparison of our results and those of Heng et al. (2011b) show, in Sect. 3.4 this effect is negligible. However, for horizontal slices at a prescribed σ this will result in the flow being presented at a different pressure surface. In effect, therefore, we assume that if a figure from Heng et al. (2011b) is presented as representative of the flow at a given σ , that actually the flow is that present at $\sigma - 1.0/(2 \times 20)$ (i.e. $\sigma - 0.025$), as Heng et al. (2011b) use 20 uniformly distributed vertical levels (with associated half-levels) spaced evenly in σ . Therefore, our Figures will be presented using the *actual* σ value of the model, where we have interpolated our prognostic variables onto this σ surface.

A2 Vertical level placements

Table A1 shows the positions of the vertical (θ)⁸, levels in non-dimensional height units (η), alongside the size of the domain H and the approximate σ value (see Sect. 3.1 for explanation).

⁸In a Charney–Phillips grid, ρ levels are placed halfway between θ levels.

Acknowledgements. This work is supported by the European Research Council under the European Community's Seventh Framework Programme (FP7/2007-2013 Grant Agreement No. 247060) and by the Consolidated STFC grant ST/J001627/1. This work is also partly supported by the Royal Society award WM090065. The calculations for this paper were performed on the DiRAC Facility jointly funded by STFC, the Large Facilities Capital Fund of BIS, and the University of Exeter.

References

- Arakawa, A. and Lamb, V. R.: Computational Design of the Basic Dynamical Processes of the UCLA General Circulation Model, in: *General Circulation Models of the Atmosphere*, edited by: Chang, J., Elsevier, *Methods in Computational Physics: Advances in Research and Applications*, 17, 173–265, doi:10.1016/B978-0-12-460817-7.50009-4, 1977. 3687
- Baraffe, I., Chabrier, G., and Barman, T.: The physical properties of extra-solar planets, *Rep. Prog. Phys.*, 73, 016901, doi:10.1088/0034-4885/73/1/016901, 2010. 3685
- Charney, J. G. and Phillips, N. A.: Numerical integration of the quasi-geostrophic equations for barotropic and simple baroclinic flows, *J. Meteorol.*, 10, 71–99, doi:10.1175/1520-0469(1953)010<0071:NIOTQG>2.0.CO;2, 1953. 3687
- Cho, J. Y.-K. and Polichtchouk, I.: The ill-effects of traditional approximation in exoplanet atmospheric flow modeling, in: *EPSC-DPS Joint Meeting 2011*, 6, EPSC-DPS2011-1536, 2011. 3685
- Cho, J. Y.-K., Menou, K., Hansen, B. M. S., and Seager, S.: Atmospheric circulation of close-in extrasolar giant planets, I. Global, barotropic, adiabatic simulations, *Astrophys. J.*, 675, 817–845, doi:10.1086/524718, 2008. 3683
- Davies, T., Cullen, M. J. P., Malcolm, A. J., Mawson, M. H., Staniforth, A., White, A. A., and Wood, N.: A new dynamical core for the Met Office's global and regional modelling of the atmosphere, *Q. J. Roy. Meteor. Soc.*, 131, 1759–1782, doi:10.1256/qj.04.101, 2005. 3685
- Hardiman, S. C., Andrews, D. G., White, A. A., Butchart, N., and Edmond, I.: Using Different Formulations of the Transformed Eulerian Mean Equations and Eliassen – Palm Diagnostics in General Circulation Models, *J. Atmos. Sci.*, 67, 1983–1995, doi:10.1175/2010JAS3355.1, 2010. 3695

Title Page

Abstract

Introduction

Conclusions

References

Tables

Figures



Back

Close

Full Screen / Esc

Printer-friendly Version

Interactive Discussion



Dynamical cores

N. J. Mayne et al.

Title Page

Abstract

Introduction

Conclusions

References

Tables

Figures



Back

Close

Full Screen / Esc

Printer-friendly Version

Interactive Discussion



- Held, I. M.: The gap between simulation and understanding in climate modeling, *B. Am. Meteorol. Soc.*, 86, 1609–1614, doi:10.1175/BAMS-86-11-1609, 2005. 3683, 3686
- Held, I. M. and Suarez, M. J.: A proposal for the intercomparison of the dynamical cores of atmospheric general circulation models, *Am. Meteorol. Soc.*, 75, 1825–1830, doi:10.1175/1520-0477(1994)075<1825:APFTIO>2.0.CO;2, 1994. 3684, 3686, 3692, 3696, 3697, 3698, 3699, 3709, 3720, 3722, 3723, 3724, 3725
- Heng, K., Frierson, D. M. W., and Phillipps, P. J.: Atmospheric circulation of tidally locked exoplanets: II. Dual-band radiative transfer and convective adjustment, *Mon. Not. R. Astron. Soc.*, 418, 2669–2696, doi:10.1111/j.1365-2966.2011.19658.x, 2011a. 3693, 3708
- Heng, K., Menou, K., and Phillipps, P. J.: Atmospheric circulation of tidally locked exoplanets: a suite of benchmark tests for dynamical solvers, *Mon. Not. R. Astron. Soc.*, 413, 2380–2402, doi:10.1111/j.1365-2966.2011.18315.x, 2011b. 3685, 3692, 3696, 3699, 3701, 3702, 3703, 3704, 3705, 3706, 3707, 3709, 3710, 3711, 3726, 3731, 3732, 3733, 3734, 3735, 3736, 3737, 3738, 3739, 3740, 3741
- Hollingsworth, J. L. and Kahre, M. A.: Extratropical cyclones, frontal waves, and Mars dust: modeling and considerations, *Geophys. Res. Lett.*, 37, L22202, doi:10.1029/2010GL044262, 2010. 3683
- Klemp, J. B. and Dudhia, J.: An upper gravity-wave absorbing layer for NWP applications, *Am. Meteorol. Soc.*, 136, 3987–4004, doi:10.1175/2008MWR2596.1, 2008. 3692, 3704
- Lebonnois, S., Lee, C., Yamamoto, M., Dawson, J., Lewis, S. R., Mendonca, J., Read, P. L., and Parish, H.: Weakly forced atmospheric GCMs: lessons from model comparisons, in: EPSC-DPS Joint Meeting 2011, 144 pp., 2011. 3683
- Lenton, T. M., Held, H., Kriegler, E., Hall, J. W., Lucht, W., Rahmstorf, S., and Schellnhuber, H. J.: Tipping elements in the Earth's climate system, *P. Natl. Acad. Sci. USA*, 105, 1786–1793, doi:10.1073/pnas.0705414105, 2008. 3683
- Melvin, T., Dubal, M., Wood, N., Staniforth, A., and Zerroukat, M.: An inherently mass-conserving iterative semi-implicit semi-Lagrangian discretization of the non-hydrostatic vertical-slice equations, *Q. J. Roy. Meteor. Soc.*, 136, 799–814, doi:10.1002/qj.603, 2010. 3692, 3704
- Menou, K. and Rauscher, E.: Atmospheric circulation of hot Jupiters: a shallow three-dimensional model, *Astrophys. J.*, 700, 887–897, doi:10.1088/0004-637X/700/1/887, 2009. 3686, 3692, 3700, 3701, 3709, 3726, 3727, 3728, 3729, 3730

Dynamical cores

N. J. Mayne et al.

Title Page

Abstract

Introduction

Conclusions

References

Tables

Figures



Back

Close

Full Screen / Esc

Printer-friendly Version

Interactive Discussion



- Merlis, T. M. and Schneider, T.: Atmospheric dynamics of Earth-like tidally locked aquaplanets, *J. Adv. Model. Earth Syst.*, 2, 13, doi:10.3894/JAMES.2010.2.13, 2010. 3686, 3692, 3703, 3709, 3732, 3734, 3735, 3736, 3737, 3738, 3739, 3740, 3741
- Müller-Wodarg, I. C. F., Mendillo, M., Yelle, R. V., and Aylward, A. D.: A global circulation model of Saturn's thermosphere, *Icarus*, 180, 147–160, doi:10.1016/j.icarus.2005.09.002, 2006. 3683
- Phillips, N. A.: Reply, *J. Atmos. Sci.*, 25, 1155–1157, doi:10.1175/1520-0469(1968)025<1155:R>2.0.CO;2, 1968. 3716
- Showman, A. P. and Guillot, T.: Atmospheric circulation and tides of “51 Pegasus b-like” planets, *Astron. Astrophys.*, 385, 166–180, doi:10.1051/0004-6361:20020101, 2002. 3685
- Showman, A. P., Fortney, J. J., Lian, Y., Marley, M. S., Freedman, R. S., Knutson, H. A., and Charbonneau, D.: Atmospheric circulation of hot Jupiters: coupled radiative-dynamical general circulation model simulations of HD 189733b and HD 209458b, *Astrophys. J.*, 699, 564–584, doi:10.1088/0004-637X/699/1/564, 2009. 3683, 3685
- Staniforth, A. and Wood, N.: The deep-atmosphere euler equations in a generalized vertical coordinate, *Am. Meteorol. Soc.*, 131, 1931–1938, doi:10.1175//2564.1, 2003. 3687, 3690
- Staniforth, A. and Wood, N.: Aspects of the dynamical core of a nonhydrostatic, deep-atmosphere, unified weather and climate-prediction model, *J. Comput. Phys.*, 227, 3445–3464, doi:10.1016/j.jcp.2006.11.009, 2008. 3687
- Thuburn, J. and Staniforth, A.: Conservation and Linear Rossby-Mode Dispersion on the Spherical C Grid, *Mon. Weather Rev.*, 132, 641–653, doi:10.1175/1520-0493(2004)132<0641:CALRDO>2.0.CO;2, 2004. 3691
- Thuburn, J., Wood, N., and Staniforth, A.: Normal modes of deep atmospheres, I: Spherical geometry, *Q. J. Roy. Meteor. Soc.*, 128, 1771–1792, doi:10.1256/003590002320603403, 2002a. 3686, 3694
- Thuburn, J., Wood, N., and Staniforth, A.: Normal modes of deep atmospheres, II: f–F-plane geometry, *Q. J. Roy. Meteor. Soc.*, 128, 1793–1806, doi:10.1256/003590002320603412, 2002b. 3686, 3694
- Ullrich, P. A., Melvin, T., Jablonowski, C., and Staniforth, A.: A baroclinic wave test case for deep- and shallow-atmosphere dynamical cores, *Q. J. Roy. Meteor. Soc.*, submitted, 2013. 3684, 3694
- Walters, D. N., Best, M. J., Bushell, A. C., Copsey, D., Edwards, J. M., Falloon, P. D., Harris, C. M., Lock, A. P., Manners, J. C., Morcrette, C. J., Roberts, M. J., Stratton, R. A., Web-

Dynamical cores

N. J. Mayne et al.

[Title Page](#)[Abstract](#)[Introduction](#)[Conclusions](#)[References](#)[Tables](#)[Figures](#)[Back](#)[Close](#)[Full Screen / Esc](#)[Printer-friendly Version](#)[Interactive Discussion](#)

ster, S., Wilkinson, J. M., Willett, M. R., Boutle, I. A., Earnshaw, P. D., Hill, P. G., MacLachlan, C., Martin, G. M., Moufouma-Okia, W., Palmer, M. D., Petch, J. C., Rooney, G. G., Scaife, A. A., and Williams, K. D.: The Met Office Unified Model Global Atmosphere 3.0/3.1 and JULES Global Land 3.0/3.1 configurations, *Geosci. Model Dev.*, 4, 919–941, doi:10.5194/gmd-4-919-2011, 2011. 3688

White, A. A. and Bromley, R. A.: Dynamically consistent, quasi-hydrostatic equations for global models with a complete representation of the Coriolis force, *Q. J. Roy. Meteor. Soc.*, 121, 399–418, doi:10.1002/qj.49712152208, 1995. 3690, 3716

White, A. A. and Wood, N.: Consistent approximate models of the global atmosphere in non-spherical geopotential coordinates, *Q. J. Roy. Meteor. Soc.*, 138, 980–988, doi:10.1002/qj.972, 2012. 3690

White, A. A., Hoskins, B. J., Roulstone, I., and Staniforth, A.: Consistent approximate models of the global atmosphere: shallow, deep, hydrostatic, quasi-hydrostatic and non-hydrostatic, *Q. J. Roy. Meteor. Soc.*, 131, 2081–2107, doi:10.1256/qj.04.49, 2005. 3685, 3687, 3690, 3691, 3717

White, A. A., Staniforth, A., and Wood, N.: Spheroidal coordinate systems for modelling global atmospheres, *Q. J. Roy. Meteor. Soc.*, 134, 261–270, doi:10.1002/qj.208, 2008. 3689

Wood, N., Staniforth, A., White, A., Allen, T., Diamantakis, M., Gross, M., Melvin, T., Smith, C., Vosper, S., Zerroukat, M., and Thuburn, J.: An inherently mass-conserving semi-implicit semi-lagrangian discretisation of the deep-atmosphere global nonhydrostatic equations, *Q. J. Roy. Meteor. Soc.*, submitted, 2013. 3684, 3685, 3686, 3687, 3688, 3689, 3691, 3694, 3707

Yamazaki, Y. H., Skeet, D. R., and Read, P. L.: A new general circulation model of Jupiter's atmosphere based on the UKMO Unified Model: three-dimensional evolution of isolated vortices and zonal jets in mid-latitudes, *Planet. Space Sci.*, 52, 423–445, doi:10.1016/j.pss.2003.06.006, 2004. 3683

Zalucha, A. M.: Demonstration of a GCM for Mars, GJ 1214b, Pluto, and Triton, *Lunar and Planetary Institute (LPI) Contributions*, 1675, 8016, 2012. 3683

Table 1. Table showing approximations made to the equations of motion (or associated geometry), the actual effect on the terms of Eq. (1) and the validity criteria. Here R_p is the radius of the planet, z is the distance from the surface of the planet, i.e. $r = z + R_p$, M_p is the mass of the planet, in this case Earth, and N is the bouyancy (or Brunt–Väisälä) frequency. *This validity criterion is from Phillips (1968), however, the validity of the “traditional” approximation is debatable and may break down for planetary scale flows (see White and Bromley, 1995, for a discussion).

Assumption	Mathematical effect	Validity
Spherical geopotentials	$\Phi(\lambda, \phi, r) = \Phi(r)$	$\Omega^2 r \ll g$
Constant gravity	$g(r) = g_{\text{surf}} = \frac{GM_p}{R_p^2}$	$z \ll R_p$
“Shallow-atmosphere”	“Shallow-fluid” $r \rightarrow R_p$ & $\frac{\partial}{\partial r} \rightarrow \frac{\partial}{\partial z}$	$z \ll R_p$
“Traditional”	$\frac{uw}{r}, \frac{vw}{r}, \frac{u^2+v^2}{r}, 2\Omega u \cos \phi, 2\Omega w \cos \phi \rightarrow 0$	$N^2 \gg \Omega^{2*}$

Title Page

Abstract

Introduction

Conclusions

References

Tables

Figures

◀

▶

◀

▶

Back

Close

Full Screen / Esc

Printer-friendly Version

Interactive Discussion



Dynamical cores

N. J. Mayne et al.

Title Page

Abstract

Introduction

Conclusions

References

Tables

Figures



Back

Close

Full Screen / Esc

Printer-friendly Version

Interactive Discussion



Table 2. Table showing the model name used in this work with the dynamical core, the name for the equation set (as described in White et al., 2005) and the main included assumptions. For a full description of the underlying equations see White et al. (2005).

Short-Name	EG _{sh}	EG _{gc}	EG	ND
Dynamical core	ENDGame	ENDGame	ENDGame	New Dynamics
White et al. (2005) model name	NHS	NHD	NHD	NHD
Spherical geopotentials	Yes	Yes	Yes	Yes
Constant gravity	Yes	Yes	No	Yes
“Shallow-atmosphere”	Yes	No	No	No

Table A1. Table showing the dimensionless vertical coordinate for the θ levels of the three model setups, η_θ ($\eta = z/H$) alongside the approximate σ levels and the model domain height (H).

Test case:		Held-Suarez (HS)	Earth-Like (EL)	Tidally Locked Earth (TLE)
H (m)		30975.0	30964.0	30056.0
Level	$\sim \sigma$	η_θ		
0	1.00	0.000000	0.000000	0.000000
1	0.97	0.009072	0.004521	0.009915
2	0.94	0.018111	0.009010	0.019763
3	0.91	0.027506	0.026967	0.029977
4	0.88	0.036901	0.036203	0.040192
5	0.84	0.046295	0.045408	0.050472
6	0.81	0.056433	0.055290	0.061951
7	0.78	0.066764	0.065495	0.073463
8	0.75	0.077094	0.075701	0.085108
9	0.72	0.088103	0.086423	0.097651
10	0.69	0.099467	0.097694	0.110194
11	0.66	0.110896	0.109030	0.123303
12	0.63	0.123099	0.121011	0.137011
13	0.60	0.135626	0.133510	0.150852
14	0.57	0.148539	0.146331	0.165824
15	0.53	0.162260	0.159928	0.180829
16	0.50	0.176303	0.174009	0.197065
17	0.47	0.191251	0.188897	0.213501
18	0.44	0.206780	0.204560	0.231302
19	0.41	0.223245	0.221128	0.249468
20	0.38	0.240613	0.238826	0.269331
21	0.35	0.259112	0.257654	0.289959
22	0.32	0.278935	0.278000	0.312018
23	0.28	0.300371	0.300026	0.336039
24	0.26	0.323584	0.324021	0.361791
25	0.22	0.349379	0.350698	0.389839
26	0.19	0.378563	0.380668	0.421047
27	0.16	0.412365	0.415321	0.456614
28	0.13	0.453010	0.457338	0.498336
29	0.10	0.504310	0.510690	0.549607
30	0.07	0.574851	0.583419	0.621540
31	0.04	0.687780	0.698908	0.736126
32	0.01	1.000000	1.000000	1.000000

Dynamical cores

N. J. Mayne et al.

Title Page

Abstract

Introduction

Conclusions

References

Tables

Figures

⏪

⏩

◀

▶

Back

Close

Full Screen / Esc

Printer-friendly Version

Interactive Discussion



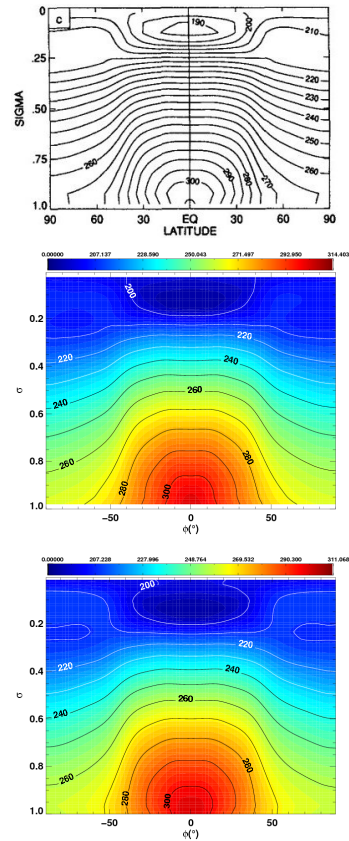


Fig. 1. Figure showing, for the Held–Suarez test (Held and Suarez, 1994), the zonally and temporally averaged (i.e. mean from 200 to 1200 days, see Sect. 3.2.1) temperature (K) as a function of latitude and σ . Top panel: original finite difference model Fig. 1 from Held and Suarez (1994), © American Meteorological Society. Used with permission. Middle panel: ND version. Bottom Panel: EG version (see Table 2 for explanation of model types).

[Title Page](#)
[Abstract](#)
[Introduction](#)
[Conclusions](#)
[References](#)
[Tables](#)
[Figures](#)

[Back](#)
[Close](#)
[Full Screen / Esc](#)
[Printer-friendly Version](#)
[Interactive Discussion](#)

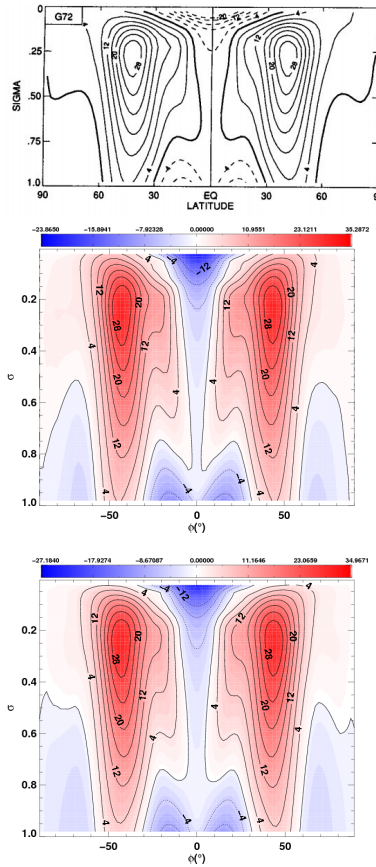



Fig. 2. Same as Fig. 1 but for zonal wind (m s^{-1}).

Title Page

Abstract

Introduction

Conclusions

References

Tables

Figures

⏪

⏩

◀

▶

Back

Close

Full Screen / Esc

Printer-friendly Version

Interactive Discussion



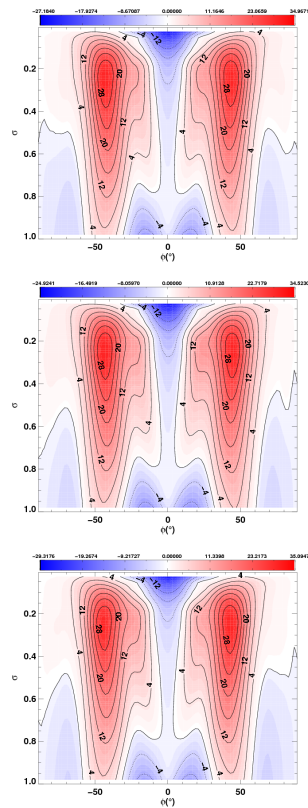


Fig. 3. Figure, for the Held–Suarez test (Held and Suarez, 1994), showing the zonally and temporally averaged zonal wind (ms^{-1}) as a function of latitude and σ . Top panel: EG model (also shown in Fig. 2 but reproduced here to aid comparison). Middle panel: EG_{gc} model. Bottom panel: EG_{sh} model (see Table 2 for explanation of model types).

[Title Page](#)
[Abstract](#)
[Introduction](#)
[Conclusions](#)
[References](#)
[Tables](#)
[Figures](#)

[Back](#)
[Close](#)
[Full Screen / Esc](#)
[Printer-friendly Version](#)
[Interactive Discussion](#)

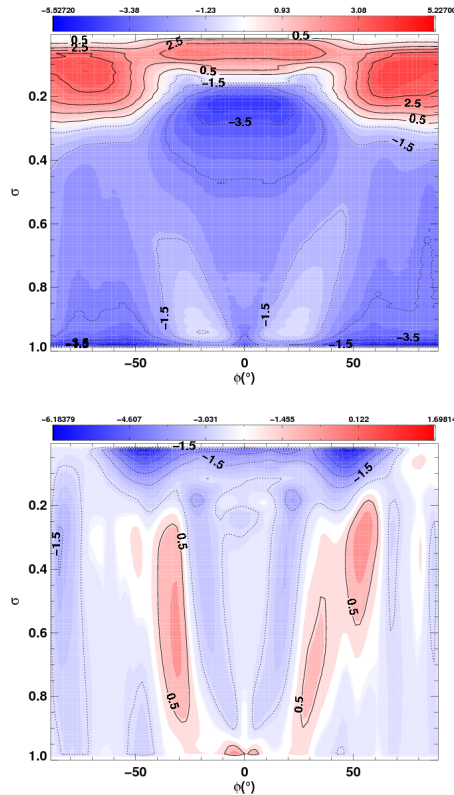



Fig. 4. Figure, for the Held–Suarez test (Held and Suarez, 1994), showing the differences EG–ND of the zonally and temporally averaged zonal temperature (K), top panel, and wind (ms^{-1}), bottom panel (see Table 2 for explanation of model types).

[Title Page](#)
[Abstract](#)
[Introduction](#)
[Conclusions](#)
[References](#)
[Tables](#)
[Figures](#)

[Back](#)
[Close](#)
[Full Screen / Esc](#)
[Printer-friendly Version](#)
[Interactive Discussion](#)


Title Page

Abstract

Introduction

Conclusions

References

Tables

Figures



Back

Close

Full Screen / Esc

Printer-friendly Version

Interactive Discussion

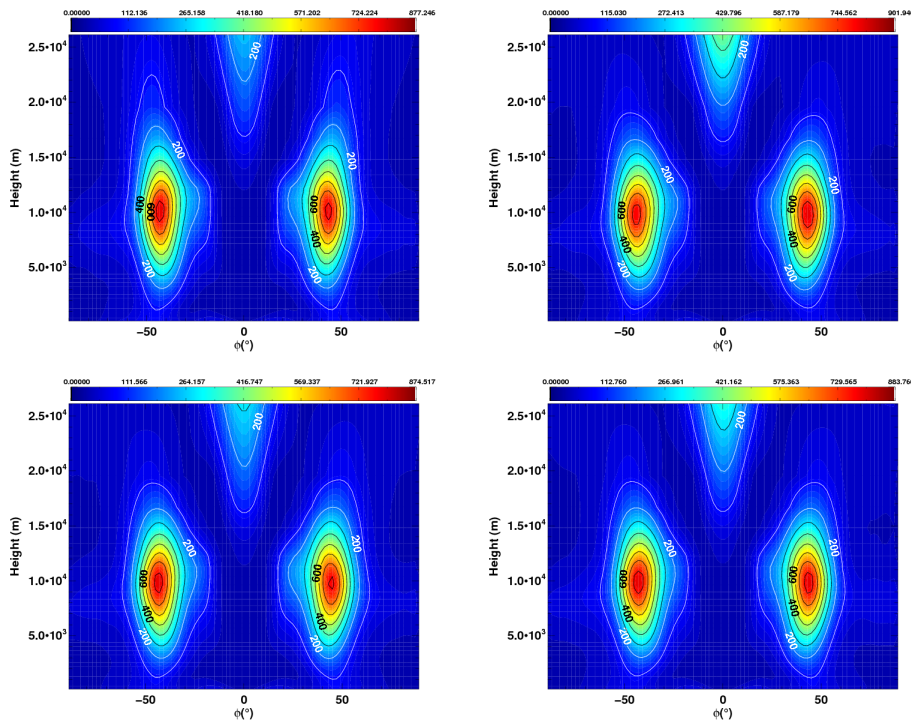


Fig. 5. Figure, for the Held–Suarez test (Held and Suarez, 1994), showing the zonally (in geometric height) and temporally averaged Eddy Kinetic Energy (EKE, see Sect. 3.1) as a function of latitude and height. Top left panel: ND, top right panel: EG_{sh} , bottom left panel: EG_{gc} and bottom right panel: EG models (see Table 2 for explanation of model types). Note the contours (solid lines) are the same in all plots.

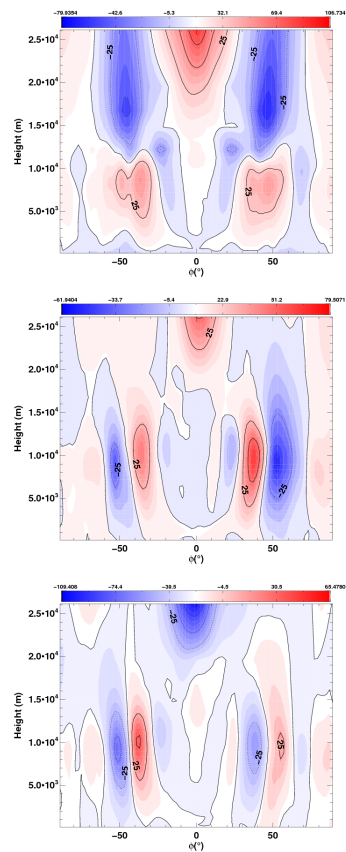


Fig. 6. Figure, for the Held–Suarez test (Held and Suarez, 1994), showing the differences EG–ND (top), EG–EG_{gc} (middle) and EG–EG_{sh} (bottom), of the zonally and temporally averaged EKE. The line contours are the same for all panels (see Table 2 for explanation of model types).

[Title Page](#)
[Abstract](#)
[Introduction](#)
[Conclusions](#)
[References](#)
[Tables](#)
[Figures](#)

[Back](#)
[Close](#)
[Full Screen / Esc](#)
[Printer-friendly Version](#)
[Interactive Discussion](#)

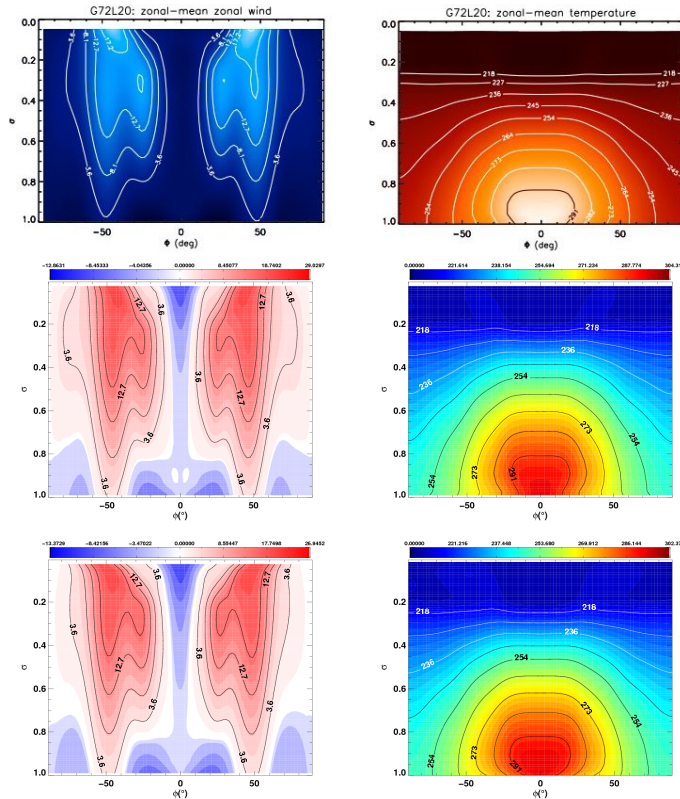



Fig. 7. Figures showing, for the Earth-like test (Menou and Rauscher, 2009), the zonally averaged temperature and zonal wind. Top panels: temporally averaged results from grid-based model of Heng et al. (2011b) (reproduced by permission of Oxford University Press). Middle and bottom panels: temporally averaged results from this work using the ND and EG models, respectively (see Table 2 for explanation of model types).

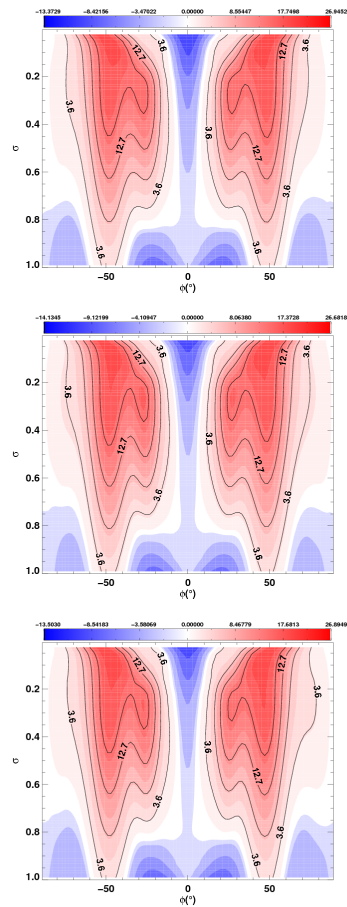


Fig. 8. Figures showing, for the Earth-like test (Menou and Rauscher, 2009), the zonally and temporally averaged zonal wind fields for the different EG models. Top panel:, EG, middle panel:, EG_{gc} and bottom panel:, EG_{sh} (see Table 2 for explanation of model types).

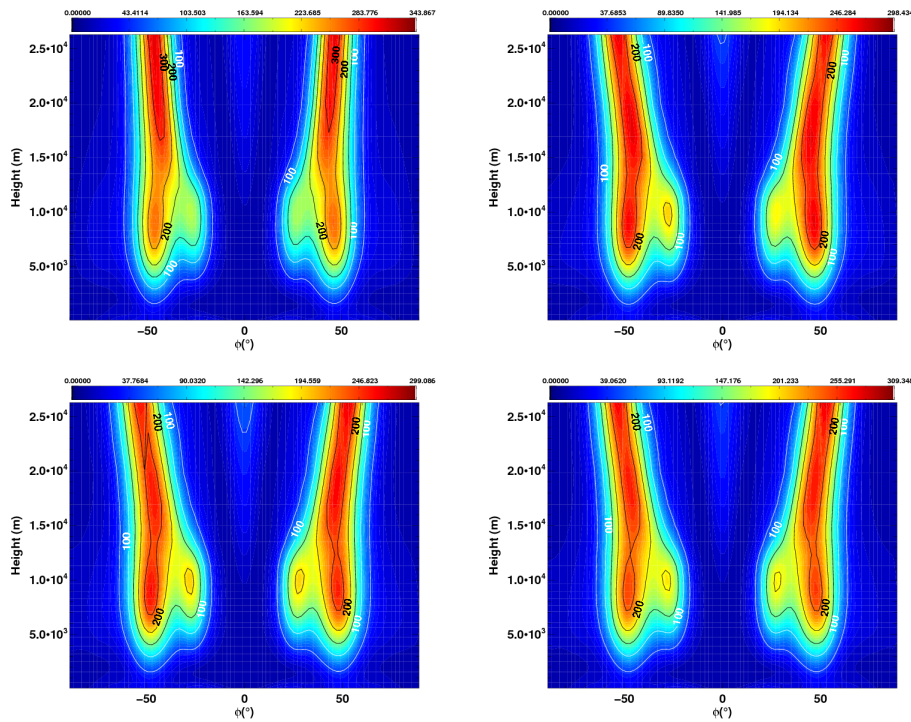


Fig. 10. Figure, for the Earth-like test (Menou and Rauscher, 2009), showing the zonally (in geometric height) and temporally averaged Eddy Kinetic Energy (EKE, see Sect. 3.1) as a function of latitude and height. Top left panel: ND, top right panel: EG_{sh} , bottom left panel: EG_{gc} and bottom right panel: EG models (see Table 2 for explanation of model types). Note the contours (solid lines) are the same in all plots.

[Title Page](#)
[Abstract](#)
[Introduction](#)
[Conclusions](#)
[References](#)
[Tables](#)
[Figures](#)

[Back](#)
[Close](#)
[Full Screen / Esc](#)
[Printer-friendly Version](#)
[Interactive Discussion](#)

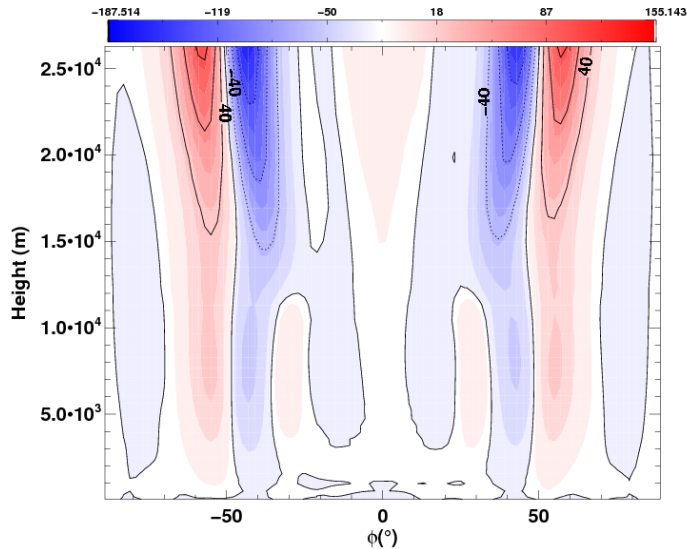



Fig. 11. Figure, for the Earth-like test (Menou and Rauscher, 2009), showing the differences EG-ND of the zonally and temporally averaged EKE (see Table 2 for explanation of model types).

Title Page

Abstract

Introduction

Conclusions

References

Tables

Figures

⏪

⏩

◀

▶

Back

Close

Full Screen / Esc

Printer-friendly Version

Interactive Discussion



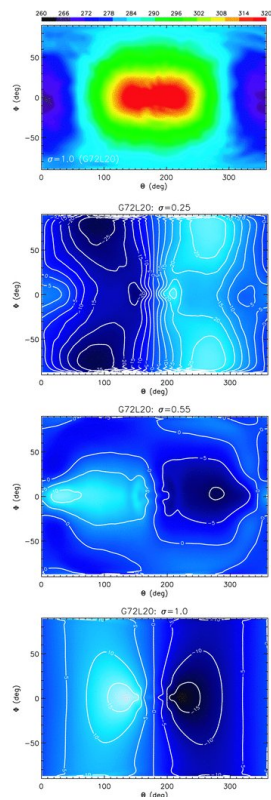


Fig. 12. Figure reproduced from Heng et al. (2011b) of the results from the grid-based model of the TLE test case (reproduced by permission of Oxford University Press). Showing (from the top panel to the bottom panel) temperature at 1200 days and $\sigma = 0.975$, then, temporally averaged zonal wind at $\sigma = 0.225$, 0.525 and 0.975 .

[Title Page](#)
[Abstract](#)
[Introduction](#)
[Conclusions](#)
[References](#)
[Tables](#)
[Figures](#)

[Back](#)
[Close](#)
[Full Screen / Esc](#)
[Printer-friendly Version](#)
[Interactive Discussion](#)

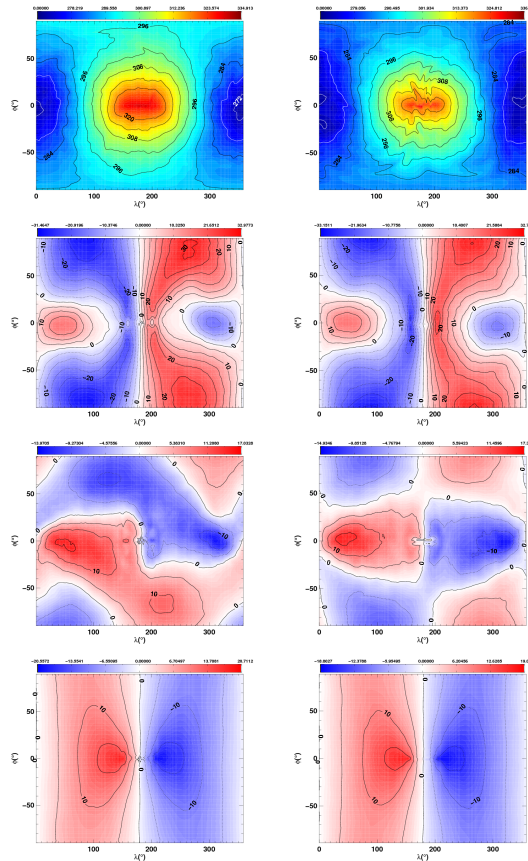



Fig. 13. Figure showing, for the Tidally Locked Earth test (Merlis and Schneider, 2010; Heng et al., 2011b), (from the top panels to the bottom panels) temperature at 1200 days and $\sigma = 0.975$, then, temporally averaged zonal wind at $\sigma = 0.225, 0.525$ and 0.975 . Results are from the ND (left panels) and EG (right panels) models (see Table 2 for explanation of model types).

[Title Page](#)
[Abstract](#)
[Introduction](#)
[Conclusions](#)
[References](#)
[Tables](#)
[Figures](#)

[Back](#)
[Close](#)
[Full Screen / Esc](#)
[Printer-friendly Version](#)
[Interactive Discussion](#)

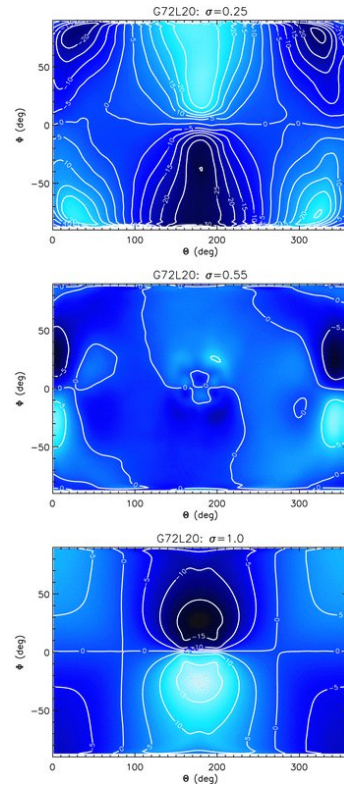



Fig. 14. Figure reproduced from Heng et al. (2011b) of the results from the grid-based model of the TLE test case (reproduced by permission of Oxford University Press). Showing (from the top panel to the bottom panel) the temporally averaged meridional wind at $\sigma = 0.225$, 0.525 and 0.975 .

[Title Page](#)[Abstract](#)[Introduction](#)[Conclusions](#)[References](#)[Tables](#)[Figures](#)[◀](#)[▶](#)[◀](#)[▶](#)[Back](#)[Close](#)[Full Screen / Esc](#)[Printer-friendly Version](#)[Interactive Discussion](#)

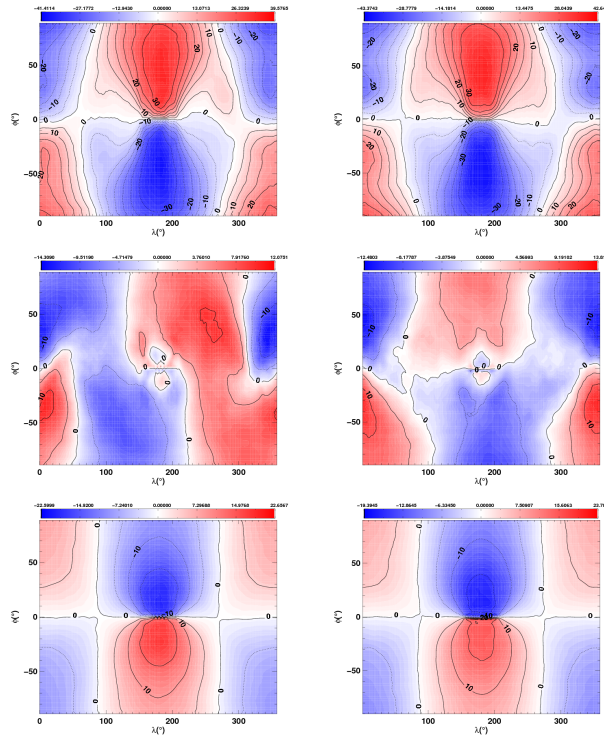


Fig. 15. Figure showing, for the Tidally Locked Earth test (Merlis and Schneider, 2010; Heng et al., 2011b), (from the top panels to the bottom panels) the temporally averaged meridional wind at $\sigma = 0.225$, 0.525 and 0.975. Results are from the ND (left panels) and EG (right panels) models (see Table 2 for explanation of model types).

[Title Page](#)
[Abstract](#)
[Introduction](#)
[Conclusions](#)
[References](#)
[Tables](#)
[Figures](#)

[Back](#)
[Close](#)
[Full Screen / Esc](#)
[Printer-friendly Version](#)
[Interactive Discussion](#)

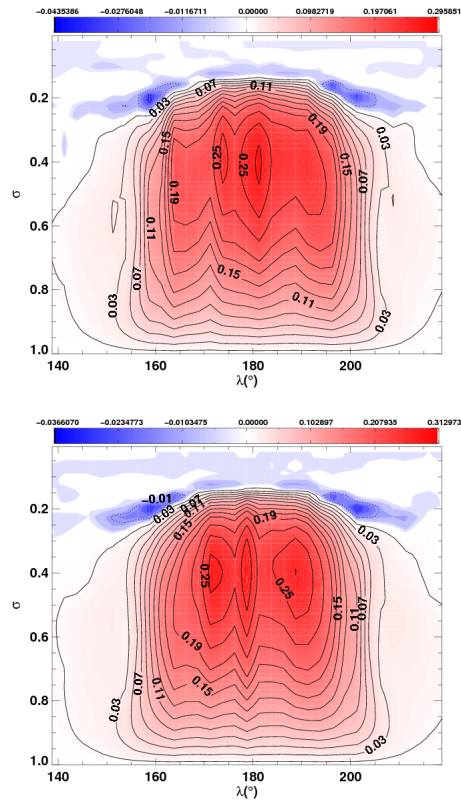



Fig. 16. Figure showing, for the Tidally Locked Earth test (Merlis and Schneider, 2010; Heng et al., 2011b), the temporally averaged vertical velocities (m s^{-1}) over the “hot spot” or subsolar point, for the ENDGame dynamical core using the EG_{sh} (top panel) and EG (bottom panel) models (see Table 2 for explanation of model types).

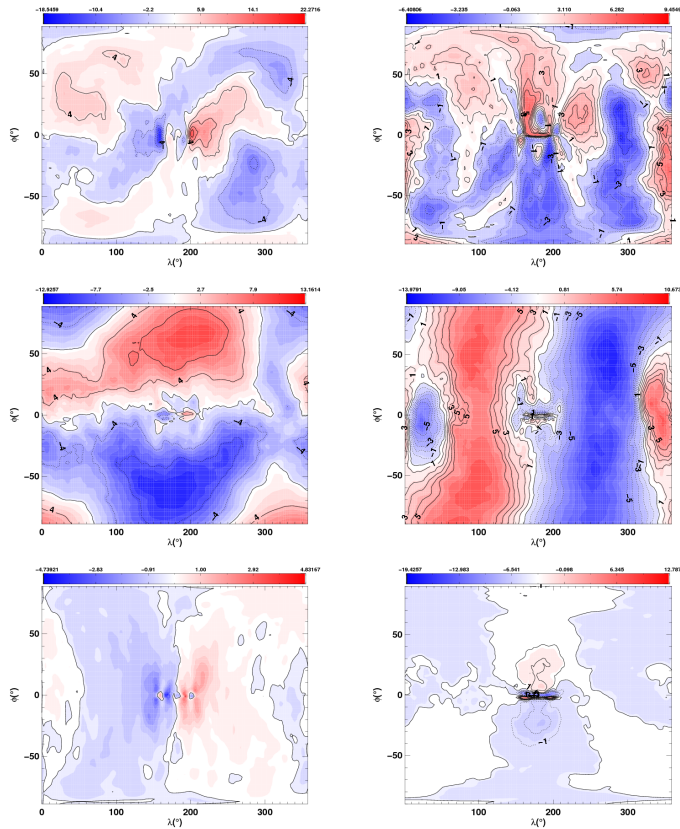


Fig. 17. Figure, Tidally Locked Earth test (Merlis and Schneider, 2010; Heng et al., 2011b), showing the differences EG–ND of the temporally averaged, zonal (left panels) and meridional (right panels) winds (m s^{-1}), at $\sigma = 0.975$, 0.525 , and 0.225 , as the top, middle and bottom rows, respectively (see Table 2 for explanation of model types).

[Title Page](#)
[Abstract](#)
[Introduction](#)
[Conclusions](#)
[References](#)
[Tables](#)
[Figures](#)

[Back](#)
[Close](#)
[Full Screen / Esc](#)
[Printer-friendly Version](#)
[Interactive Discussion](#)

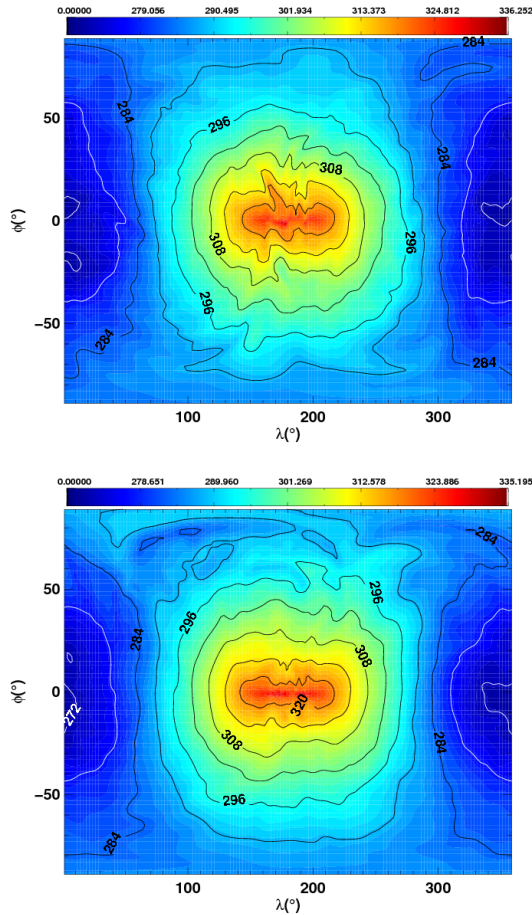



Fig. 18. Figure showing, for the Tidally Locked Earth test (Merlis and Schneider, 2010; Heng et al., 2011b), showing temperature at 1200 days and $\sigma = 0.975$, for the EG models (see Table 2 for explanation of model types) using α of 0.55 and 1.0 (top and bottom panels, respectively).

Title Page

Abstract

Introduction

Conclusions

References

Tables

Figures

◀

▶

◀

▶

Back

Close

Full Screen / Esc

Printer-friendly Version

Interactive Discussion



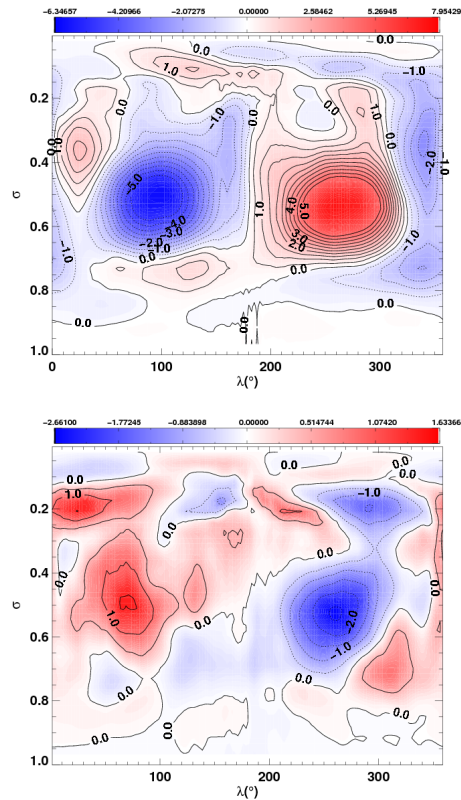


Fig. 19. Figure showing, for the Tidally Locked Earth test (Merlis and Schneider, 2010; Heng et al., 2011b), the temporally and meridionally averaged meridional flow for the ND (top panel) and EG_{gc} (bottom panel) models (see Table 2 for explanation of model types).

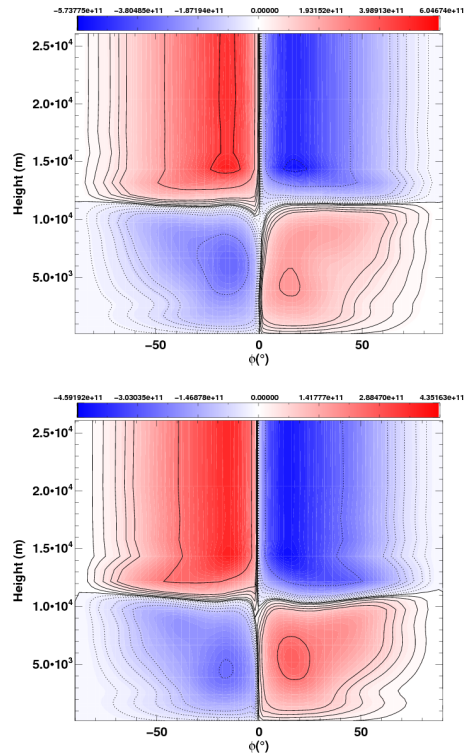


Fig. 20. Figure showing, for the Tidally Locked Earth test (Merlis and Schneider, 2010; Heng et al., 2011b), the streamfunction Ψ (defined in text, see Eq. 20) for the ND (top panel) and EG_{gc} (right panel) models (see Table 2 for explanation of model types). The contours in both panels are the same and set at values -5.0×10^{11} , -2.5×10^{11} , -1.0×10^{11} , -7.5×10^{10} , -5.0×10^{10} , -2.5×10^{10} , -1.0×10^{10} , 0.0 , 1.0×10^{10} , 2.5×10^{10} , 5.0×10^{10} , 7.5×10^{10} , 1.0×10^{11} , 2.5×10^{11} and 5.0×10^{11} .

[Title Page](#)
[Abstract](#)
[Introduction](#)
[Conclusions](#)
[References](#)
[Tables](#)
[Figures](#)
[◀](#)
[▶](#)
[◀](#)
[▶](#)
[Back](#)
[Close](#)
[Full Screen / Esc](#)
[Printer-friendly Version](#)
[Interactive Discussion](#)

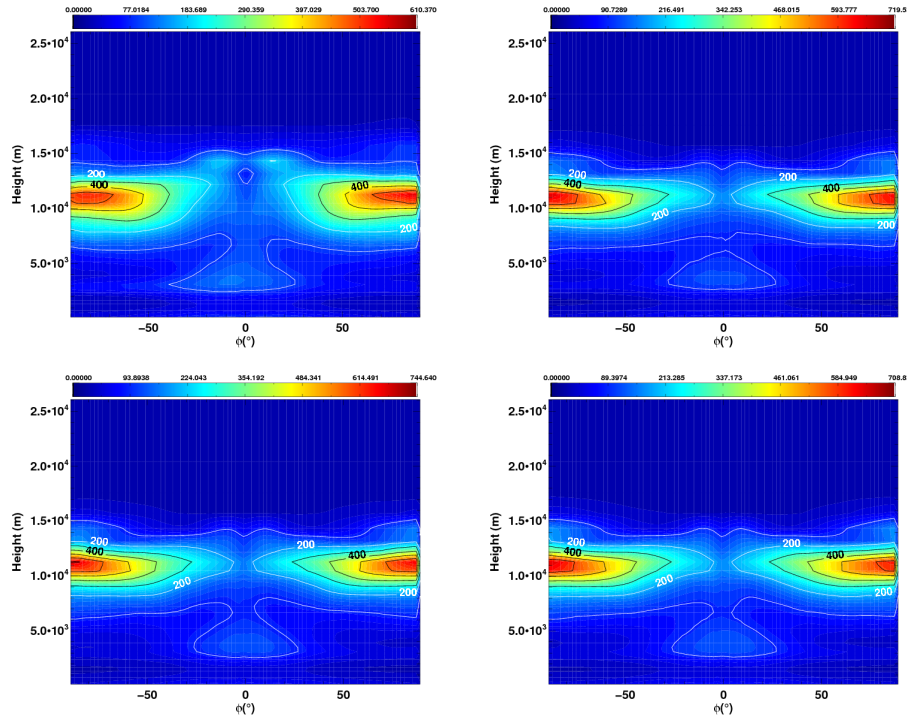



Fig. 21. Figure, for the Tidally Locked Earth test (Merlis and Schneider, 2010; Heng et al., 2011b), showing the zonally (in geometric height) and temporally averaged Eddy Kinetic Energy (EKE, see Sect. 3.1) as a function of latitude and height. Top left panel ND, top right panel: EG_{sh} , bottom left panel: EG_{gc} and bottom right panel: EG models (see Table 2 for explanation of model types). Note the contours (solid lines) are the same in all plots.

Title Page

Abstract

Introduction

Conclusions

References

Tables

Figures

⏪

⏩

◀

▶

Back

Close

Full Screen / Esc

Printer-friendly Version

Interactive Discussion



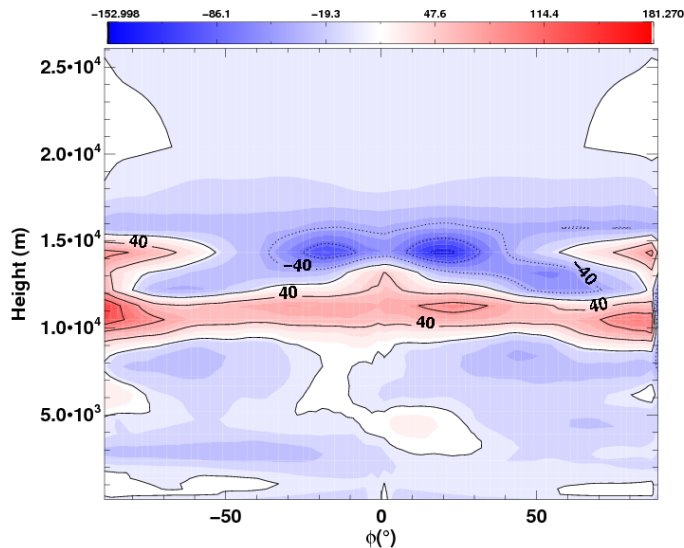


Fig. 22. Figure, for the Tidally Locked Earth test (Merlis and Schneider, 2010; Heng et al., 2011b), showing the differences EG-ND of the zonally and temporally averaged EKE (see Table 2 for explanation of model types).

[Title Page](#)
[Abstract](#)
[Introduction](#)
[Conclusions](#)
[References](#)
[Tables](#)
[Figures](#)
[⏪](#)
[⏩](#)
[◀](#)
[▶](#)
[Back](#)
[Close](#)
[Full Screen / Esc](#)
[Printer-friendly Version](#)
[Interactive Discussion](#)
